



## AN ABSTRACT OF THE THESIS OF

Sebastian Okhovat for the degree of Master of Science in Mechanical Engineering presented on December 9, 2015.

Title: Temperature Evolution of Spark Kernels in Quiescent and Cross-flow Conditions.

Abstract approved: \_\_\_\_\_

David L. Blunck

Numerous physical and chemical processes are required for successful ignition of a flammable mixture, many of which have been well characterized. However, one aspect of the ignition process that has received limited consideration is understanding the temperature of the spark kernel. A spark kernel is the volume of heated gas that develops after plasma formation and dissipation by an electrical discharge. Thermal measurements are critical for determining if reactions become self-sustaining and improving the validity of modeling efforts. The need for quantified kernel temperatures is extended to conditions that approach the flow fields within combustion applications, such as gas turbine engines. Based on the motivation, the focus of this work was to determine the temperature of kernels and investigate the influence a cross-flow has on the temporal temperature evolution. Representative results were compared against kernel temperatures in a quiescent environment to highlight differences between the two flow conditions. In this study, a sunken fire igniter was placed in an open loop wind tunnel and discharged into a non-reacting cross-flow. Kernel temperatures, after the plasma dissipated, were determined from radiation intensity measurements and by solving the radiation transfer equation. The temperature evolution was investigated in a quiescent environment and for a range of cross-flow velocities (5.8-15.6 m/s). For both quiescent and cross-flow conditions, kernels developed into a toroidal vortex. Surrounding air was entrained into the center of the kernel, resulting in relatively lower temperatures compared to the edges. Average peak kernel temperatures in quiescent conditions were 950 K, whereas kernels in a cross-flow approached 1250 K. The higher peak temperatures were attributed to a reduced relative velocity of the vortex caused by the interaction with the cross-flow. This resulted in decreased entrainment, particularly located at the upstream side of the kernel.

Most of the temperature evolution of kernels was experienced within 1.3 ms after plasma was no longer detected; up to a 500 K difference was determined between 0.6 and 1.3 ms. Kernels beyond 1.3 ms reached a uniform temperature near 600 K and had little to no variation as radiation intensities dissipated beyond optical detection. Bifurcation of kernels was detected in one-third of all spark events for both quiescent and cross-flow conditions. The sensible energy of kernels was reported to decrease with time for all cases. Higher cross-flow velocities resulted in less sensible energy. This was attributed to a reduction in apparent kernel volume even with higher temperatures.

©Copyright by Sebastian Okhovat  
December 9, 2015  
All Rights Reserved

Temperature Evolution of Spark Kernels in Quiescent and Cross-flow Conditions

by  
Sebastian Okhovat

A THESIS

submitted to

Oregon State University

in partial fulfillment of  
the requirements for the  
degree of

Master of Science

Presented December 9, 2015  
Commencement June 2016

Master of Science thesis of Sebastian Okhovat presented on December 9, 2015

APPROVED:

---

Major Professor, representing Mechanical Engineering

---

Head of the School of Mechanical, Industrial, and Manufacturing Engineering

---

Dean of the Graduate School

I understand that my thesis will become part of the permanent collection of Oregon State University libraries. My signature below authorizes release of my thesis to any reader upon request.

---

Sebastian Okhovat, Author

## ACKNOWLEDGEMENTS

I would like to express my sincere appreciation and gratitude to my advisor and mentor Dr. David L. Blunck. His experiences and teachings have helped further my skills as a researcher and communicator. I would like to thank him for his patience, dedication, and trust during my time as a graduate student. Also, I would like to recognize Dr. Blunck and family for their kindness and openness outside of academics.

Many thanks to Dr. Nancy Squires for her invaluable advice, career opportunities, and support since my junior year at Oregon State University. Without your contributions, I might not be in a position to write a master's thesis.

To my close friends Mr. Firas Siala and Mr. Alexander Totpal, thank you for all the countless memories and adventures in and outside of Rogers Hall. Thank you for the encouragement to pursue graduate school, especially Firas for smacking some sense into me when I thought I was not cut out for graduate school.

Thank you to all my friends and family for believing in me and allowing me to follow my passions without squabble. The engineering lifestyle does not just affect the student, it can also take a toll on those around them. I cannot even imagine how you put up with my lack of attendance at social gatherings. I guess it must be my good looks.

Lastly, I would like to extend my thanks to members of the Combustion, Ignition, Radiation, and Energy (CIRE) Laboratory for their assistance and advice along the way.

## TABLE OF CONTENTS

|        |  |           |
|--------|--|-----------|
| 1.     | Introduction.....  | 1         |
| 1.1    | Motivation .....   | 1         |
| 1.2    | Overall Objective .....  | 2         |
| 2.     | Literature Review.....   | 3         |
| 2.1.   | Ignition .....   | 3         |
| 2.2.   | Spark Kernels .....  | 4         |
| 2.2.1. | <i>Spatial and Temporal Development.....</i>                   | <i>5</i>  |
| 2.2.2. | <i>Temperature Development.....</i>                            | <i>7</i>  |
| 2.3.   | Vortex Rings .....   | 9         |
| 3.     | Experimental Methodology .....                                 | 11        |
| 3.1.   | Arrangement.....   | 11        |
| 3.2.   | Radiation Intensity Measurements .....                         | 14        |
| 3.3.   | Deconvolution Technique .....                                  | 16        |
| 3.4.   | Evaluation of Technique .....                                  | 18        |
| 3.4.1. | <i>Temperature Comparison against Calibration Burner .....</i> | <i>18</i> |
| 3.4.2. | <i>Sensitivity Analysis.....</i>                               | <i>22</i> |
| 3.5.   | Sensible Energy.....   | 23        |
| 4.     | Results and Discussion .....                                   | 25        |
| 4.1.   | Quiescent Conditions .....                                     | 25        |
| 4.1.1. | <i>Kernel Development and Bifurcation .....</i>                | <i>25</i> |
| 4.1.2. | <i>Voltage Dependence .....</i>                                | <i>27</i> |
| 4.1.3. | <i>Temperature Results .....</i>                               | <i>28</i> |
| 4.1.4. | <i>Trajectory.....</i>   | <i>30</i> |
| 4.2.   | Cross flow Conditions.....                                     | 32        |
| 4.2.1. | <i>Kernel Development.....</i>                                 | <i>32</i> |

TABLE OF CONTENTS (CONTINUED)

|   |    |
|---|----|
| 4.2.2. <i>Temperature Results</i> .....     | 33 |
| 4.2.3. <i>Trajectory</i> .....              | 35 |
| 4.2.4. <i>Sensible Energy Results</i> ..... | 36 |
| 5. Summary and Conclusions .....            | 38 |
| References.....                             | 40 |

## LIST OF FIGURES

| <u>Figure</u>   | <u>Page</u> |
|---|-------------|
| Figure 1: Circuit schematic of igniter to determine supplied energy.....  | 12          |
| Figure 2: Experimental arrangement for investigating spark discharges into quiescent and cross-flow environments .....                                      | 13          |
| Figure 3: Path length estimate for spark kernels.....   | 17          |
| Figure 4: Radial temperature profile of McKenna burner ( $\Phi=1.05$ ). .....   | 21          |
| Figure 5: Comparison of thermocouple and deconvoluted temperatures of McKenna burner flame.<br>.....  | 22          |
| Figure 6: Sensitivity of temperature with variation in key parameters.....  | 23          |
| Figure 7: Time resolved emissions from a representative spark kernel.....   | 25          |
| Figure 8: Images of kernel progression into toroidal structure from off axis top view. ....   | 26          |
| Figure 9: Kernel development leading to bifurcation. ....   | 26          |
| Figure 10: Line-of-sight images showing trailing column from kernel development. ....   | 27          |
| Figure 11: Average kernel temperatures from roughly 100 spark events.....   | 28          |
| Figure 12: Phase averaged kernel temperatures.....  | 28          |
| Figure 13: Average temperature of kernels in a quiescent environment .....  | 30          |
| Figure 14: Trajectory of kernels in a quiescent environment .....   | 31          |
| Figure 15: Kernel velocity in a quiescent environment .....   | 31          |
| Figure 16: Raw instantaneous intensity of kernels in a 5.8 m/s (top) and 15.6 m/s (bottom) cross-flow. ....   | 32          |
| Figure 17: Phase averaged kernels in a cross-flow velocity of 5.8 m/s (top), 11.2 m/s (middle), and 15.6 m/s (bottom). Flow is left to right. ....          | 33          |
| Figure 18: Illustration of kernel interaction with cross-flow.....  | 34          |
| Figure 19: Average temperatures for kernels in 5.8 m/s (left), 11.2 m/s (middle), and 15.6 m/s (right) cross-flow velocity.....                             | 35          |
| Figure 20: Kernel trajectory compared against an elevated pulsed jet for 5.8 m/s (left), 11.2 m/s (middle), and 15.6 m/s (right) cross-flow velocities..... | 36          |
| Figure 21: Sensible energy of spark kernels for quiescent and cross-flow conditions.....  | 37          |

## LIST OF TABLES

| <u>Table</u>                                   | <u>Page</u> |
|--|-------------|
| Table 1: Fuels considered in MIE research..... | 3           |

## LIST OF APPENDICES

| <u>Appendix</u>   | <u>Page</u> |
|---|-------------|
| Appendix A: Integration Time Calculations.....                                | 47          |
| Appendix B: Spectral Absorption of Optical Equipment .....                    | 48          |
| Appendix C: Psychrometric and Chemical Composition Analysis .....             | 49          |
| Appendix D: Interpolation Database Code.....                                  | 50          |
| Appendix F: Deconvolution of Intensity to attain Temperature (DIT) Code ..... | 53          |
| Appendix E: Additional Post Processing Codes.....                             | 60          |

## LIST OF SYMBOLS

### Abbreviations

|               |                                 |
|---------------|---------------------------------|
| <i>conv</i>   | Convection                      |
| <i>GTE</i>    | Gas turbine engine              |
| <i>IR</i>     | Infrared                        |
| <i>MIE</i>    | Minimum ignition energy         |
| <i>NaN</i>    | Not a number                    |
| <i>OEM</i>    | Original equipment manufacturer |
| <i>rad</i>    | Radiation                       |
| <i>SE</i>     | Standard error                  |
| <i>stoich</i> | Stoichiometric                  |
| <i>TC</i>     | Thermocouple                    |

### Greek Symbols

|                  |  |
|------------------|--|
| $\alpha$         | Spectral absorptivity                                    |
| $\varepsilon$    | Emissivity   |
| $\lambda$        | Wavelength, $\mu\text{m}$                                |
| $\kappa_\lambda$ | Absorption coefficient, $\text{m}^{-1}$                  |
| $\mu_f$          | Dynamic viscosity of flame, $\text{kg/m}\cdot\text{s}$   |
| $\Phi$           | Equivalence ratio  |
| $\rho$           | Density, $\text{kg/m}^3$                                 |
| $\sigma$         | Stefan-Boltzmann constant, $\text{W/m}^2\cdot\text{K}^4$ |
| $\sigma_{stat}$  | Standard deviation                                       |
| $\tau_\lambda$   | Optical thickness at point of emission                   |
| $\tau_\lambda^*$ | Optical thickness at point of interest                   |

### Roman Symbols

|       |   |
|-------|---|
| $A_s$ | Surface area, $\text{m}^2$                |
| $c_p$ | Specific heat, $\text{J/kg}\cdot\text{K}$ |
| $D$   | Diameter of igniter, $\text{m}$           |

## LIST OF SYMBOLS (CONTINUED)

|                 |  |
|-----------------|--|
| $D_{TC}$        | Diameter of thermocouple, m                              |
| $E$             | Supplied energy, J                                       |
| $h_{conv}$      | Heat transfer coefficient, W/m <sup>2</sup> -K           |
| $\Delta h$      | Differential height, m                                   |
| $I$             | Integrated intensity, W/m <sup>2</sup> -sr               |
| $I_{\lambda}$   | Spectral intensity, W/m <sup>2</sup> -sr- $\mu\text{m}$  |
| $I_{b,\lambda}$ | Blackbody intensity, W/m <sup>2</sup> -sr- $\mu\text{m}$ |
| $I_{DC}$        | Direct current, A  |
| $m$             | Mass, kg   |
| $\dot{m}$       | Mass flow rate, kg/s                                     |
| $n$             | Statistical relevant parameter                           |
| $Nu$            | Nusselt number   |
| $P$             | Pressure, Pa   |
| $Pr$            | Prandtl number   |
| $Q$             | Heat, W  |
| $R$             | Universal gas constant for air, J/kg-K                   |
| $R_{C.F.}$      | Cross-flow velocity ratio                                |
| $Re_{D_{TC}}$   | Reynolds number across thermocouple                      |
| $s$             | Path length, m   |
| $T$             | Temperature, K   |
| $T_{actual}$    | Raw computed temperature (sensitivity analysis only), K  |
| $T_{adjusted}$  | Adjusted temperature (sensitivity analysis only), K      |
| $T_f$           | Flame temperature, K                                     |
| $T_{TC}$        | Thermocouple temperature, K                              |
| $T_{\infty}$    | Ambient temperature, K                                   |
| $\Delta T$      | Change in temperature, K                                 |
| $\Delta T_{SA}$ | Change in temperature (sensitivity analysis only), K     |
| $U$             | Sensible energy, J                                       |
| $V$             | Volume, m <sup>3</sup>                                   |

LIST OF SYMBOLS (CONTINUED)

|            |                                     |
|------------|-------------------------------------|
| $V_{C.F.}$ | Cross-flow velocity, m/s            |
| $V_{DC}$   | Voltage, V                          |
| $V_{jet}$  | Ejected kernel velocity, m/s        |
| $V_{mix}$  | Fuel-air mixture velocity, m/s      |
| $\bar{X}$  | Centroid location in $x$ -direction |
| $\bar{Y}$  | Centroid location in $y$ -direction |

# 1. Introduction

## 1.1 Motivation

Consistent and reliable ignition of gas turbine engines (GTE) is needed for both industrial and aviation applications. Ignition for GTEs will become more challenging as industries and government organizations pursue alternative fuels or change operation envelopes (i.e., fuel-lean combustion). This is especially pertinent to aviation GTEs because of safety implications. High altitude engine relight might become more difficult and flame blowout may occur more frequently under the proposed changes (i.e., alternative fuels, operation envelopes) [1]. Thus, it is important to understand and study ignition to continue advancing GTE technology.

Two approaches are commonly used to study ignition: investigating the minimum ignition energy (MIE) and characterizing a spark kernel. MIE research aims to determine the minimum energy needed to ignite a mixture, which includes quantifying the quenching distance and understanding the chemical kinetics. Another approach to consider for studying ignition has been the development of spark kernels. A spark kernel is a small volume of heated gas resulting from a spark discharge [2]. Understanding the formation and response of kernels can lead to improved ignition performance under difficult operating conditions (i.e., lean fuel-air ratios) [3].

MIE values have been determined for numerous transportation fuels including n-octane, propane, Jet-A, and kerosene [4–7]. A majority of the contributions from MIE research have been at quiescent conditions. Glassman noted that a flowing mixture will require a higher MIE compared to a stagnant mixture [8]. Thus, such ignition energies depend on the flow conditions, which can be one of the challenges with MIE research.

Studies of spark kernels have typically focused on their spatial and temporal development [9–16] for a wide range of time scales (i.e., 1  $\mu$ s to 5 ms). Such information provides the location of the kernels, which is important during the design process of a GTE. Characterization of the kernel could lead to a reduction in the number of igniters used in a combustor [17]. Maximized exposure to the kernel with appropriate placement of the fuel spray nozzle could increase the effectiveness of ignition. Conversely, not accounting for the kernel's trajectory may expose it to adverse effects (i.e., increased turbulence, limited exposure to flammable mixture in combustor).

Additional insight into the ignition process can be gained by quantifying the temperature of spark kernels [10,11,18,19]. The temperature of the gases is critical to determining if reactions become self-sustaining. Reaching the reaction temperature is an important aspect for implementing “drop in” alternative fuels [20], and determining kernel temperature contours for specific OEM igniters may accelerate their use.

Despite the significance, little research has focused on the temperature of spark kernels. Moreover, three out of the four research groups that have determined temperatures only considered quiescent conditions. This is significant because it does not consider flow fields representative of a GTE combustor. The previous investigation of spark kernels in such a flow field was only performed for a single cross-flow velocity. Furthermore, kernel temperatures have not been assessed for reacting conditions, primarily because of challenges associated with complex fuel chemistry.

## **1.2 Overall Objective**

Considering the importance of the temperature in the ignition process and the limited measurements of spark kernel temperatures, the objectives of this work are as follows:

- 1) Determine the spatiotemporal development of kernels under quiescent and cross-flow conditions
- 2) Determine the temperature of spark kernels under quiescent and cross-flow conditions;
- 3) Measure the trajectory of kernels; and
- 4) Quantify the sensible energy of kernels.

It should be mentioned that the focus of this work is not on studying ignition; rather, it establishes fundamental understanding for ignition mechanisms.

## 2. Literature Review

### 2.1. Ignition

Ignition is a multidimensional and time dependent process said to be more complex than other classical combustion phenomenon [21]. Spontaneous and forced ignition are two well studied types. The former can occur by fast chain branching (i.e., explosion) or slow exothermal decomposition [8]. Forced ignition occurs as a result of gas-phase reactions that are induced by an external energy source [8]. Typically, spontaneous ignition is associated with surpassing a critical temperature and/or pressure limit of a reactive material [22]. Forced ignition, however, requires an external source of energy to cause ignition and is primarily associated with gaseous mixtures [8]. Pilot flames or electrical discharges are needed to initiate chemical breakdown of the gaseous mixture. A self-propagating flame front develops and consumes the remaining volatile gases if the energy source is sufficient enough. Otherwise, the rate of chemical breakdown will decline and the initial source of energy will extinguish.

One of the metrics used to investigate and better understand forced ignition is the minimum ignition energy (MIE), which is the minimum energy required to ignite a mixture. Such studies have led to extensive databases that are both fuel and concentration dependent. Table 1 is a list of some of the various fuels that have been investigated.

Table 1: Fuels considered in MIE research

| <b>Literature</b>   | <b>Year</b> | <b>Fuel Considered</b>               |
|---------------------|-------------|--------------------------------------|
| Coudour et al. [23] | 2015        | $\alpha$ -Pinene, benzene            |
| Peng et al. [16]    | 2013        | Methane                              |
| Bane et al. [6]     | 2013        | Kerosene, <i>n</i> -hexane, hydrogen |
| Tihay et al. [24]   | 2012        | Acetone                              |
| Eckhoff et al. [4]  | 2010        | Propane                              |
| Kondo et al. [25]   | 2003        | n-Butane, ethylene,                  |
| Lee et al. [5]      | 2001        | Propane, dodecane, Jet-A             |

Lee et al. [5] investigated the influence of pressure on the MIE of a quiescent propane, dodecane, and Jet-A for a range of equivalence ratios (e.g., 0.4-2). MIE values for propane and dodecane were found to increase at sub-atmospheric pressures (e.g., <1 atm) for each equivalence ratio. Additionally, the lowest MIE value was determined at fuel-rich conditions. Similar results were measured when considering Jet-A. This was a significant finding considering that it suggests more input energy and fuel may be required for high altitude engine relight in aviation GTEs.

Typically, MIE database values are regarded as standards [4,7], where members of the combustion community can look up the value specific to their application. However, discrepancies in the measurements for the same fuels and concentrations have been documented [4,26]. The classical work by Lewis and von Elbe [26] arrived at an MIE of 0.25 mJ for 5.2 volume percent propane. Yet, Eckhoff et al. [4] later determined that that value was overly conservative, and was revised to 0.48 mJ. Bane et al. [6] learned that at atmospheric pressure and near 330 K, the probability of igniting seven volume percent hydrogen was approximately 25 percent at or greater than the specified MIE value. This highlights that ignition is not guaranteed to occur at the MIE or greater conditions.

As mentioned previously, MIE research has typically been approached using a stagnant mixture. However, a higher MIE is required for equivalent mixtures that are flowing [8]. This occurs because the spark elongates in the direction of the flow, causing the initial input energy to be distributed across a larger volume [8]. Therefore, more input energy is required to compensate for the larger cross-sectional area [21].

Despite the challenges, MIE research has established fundamental concepts that are important in the combustion community. However, an alternative approach might be needed to gain further understanding into ignition.

## **2.2. Spark Kernels**

Another metric for studying ignition is quantifying spark kernels. There are two facets of this research, which includes the fluid mechanic development of kernels and the temperature evolution of kernels. Understanding how the kernel spatially and temporally develops is of great importance for combustion devices, particularly considering dynamic flow fields. The temperature of spark kernels can provide additional insights into the ignition process that may not necessarily be

determined from spatial and temporal findings. According to Jost [27], “more exact” results can be obtained from temperature development studies.

### *2.2.1. Spatial and Temporal Development*

Sforzo et al. [18] studied kernels experimentally and numerically exiting into a uniform cross-flow (33 m/s) of air. High speed schlieren and emission imaging was used to visualize kernels. The numerical approach encompassed the fully compressible Navier-Stokes equation, coupled with the conservation of mass, species, and energy relations. The assumption of thermal equilibrium within the spark volume was needed to solve the equations. A dielectric gap between co-linear copper electrodes was used to generate kernels. The initial shape of kernels after discharge (e.g., 60  $\mu\text{s}$ ) was near-cylindrical, but later developed into a toroid within 100  $\mu\text{s}$ . The group assumed that the center void was equal to one-third of the outer diameter of the toroid. The development of the toroid allows surrounding air to be entrained into the kernel, which resulted in a roughly 25 percent increase in the kernel’s cross-sectional area between 0.6 and 200  $\mu\text{s}$ . The group noted that splitting of the toroid preferentially occurred at the upstream side; it was attributed to an effect by the electrode. However, further discussion of why the electrode influenced the splitting was not mentioned. It was concluded that their experimental and numerical results were in good agreement with each other, with slight deviations in the predicted size of kernels. It was postulated that the edge detection used in the experimental effort was accounting for additional fluid that was not necessarily from the kernel, thereby resulting in a larger kernel.

The work by Eisazadeh-Far et al. [12] compared the development of kernels discharged in quiescent air against a quiescent methane/air mixture. Stainless steel electrodes were separated by a 1 mm gap and placed in a combustion chamber. Kernels in ambient air and methane/air, both at 1 atm and 300 K, were spherical in shape and exhibited similar spatial developments within 1 ms. A fourfold radius increase was observed for both conditions between 0.1-1 ms after spark discharge. Between 1 and 2 ms, air kernels were reported to be “stable” (i.e., no additional growth), whereas methane/air kernels experienced rapid growth. It was mentioned that the contributions of the kernel on the chemical and transport processes were not significant until 1-2 ms after spark discharge. Eisazadeh-Far et al. concluded that the volume and temperature of kernels, based on

their experimental arrangement, was dependent on the electrical energy that was supplied; more energy resulted in larger volumes and higher temperatures.

Eichenberger and Roberts [28] investigated spark kernels at a constant methane/air mixture ( $\Phi=0.55$ ) using two electrodes separated by a 2 mm gap. Their objective was to study the effects of a turbulent flow field on the fluid mechanic development of kernels. This was accomplished by generating a vortex ring, of known length and time scales, and ejecting it in the direction of the electrodes such as to collide with the kernel. An amalgamation was observed between the kernel and vortex ring within 1 ms of ignition of methane. The kernel took on the form of the vortex as the dominating structure. It can be inferred from these results that hot gases were contained in the vortex ring. The kernel would most likely develop spherically without the vortex ring, which is similar to the results by Eisazadeh-Far et al. [12]. This is highly probable because of the near identical electrode configuration between the two groups. The inertia of the initial propagating ring was found to advect the kernel-vortex away from the electrodes. Eichenberger and Roberts suggested that the detachment from the electrodes may reduce the heat losses of the kernel. Increasing the rotational velocity of the vortex led to localized quenching of the reactive kernel, but no extinguishment was detected. Further increases in the rotational velocity ultimately resulted in global quenching within 5 ms after ignition occurred. The reasoning behind kernel quenching was not fully discussed, rather observational inferences were mentioned.

Spark kernels discharged from a pulse plasma igniter were measured under quiescent air conditions by Blunck et al. [10]. Radiation intensity measurements revealed that the kernel developed into a toroidal vortex within 1.6 ms of discharge. Heated gas was ejected from the tip of the igniter, followed by the emergence of the vortex. This led to entrainment of surrounding fluid into the center. Additionally, a “tail” of radiation emissions was observed for kernels discharged with a pulsed plasma igniter. Kernels were determined to propagate, on average, 2.5 cm vertically above the igniter. It is worth mentioning that kernels with this type of igniter exhibited non-buoyant tendencies at the investigated time scale (on the order of ms). This was determined by orienting the igniter parallel with the ground and visualizing if kernels rose with respect to the horizon [10]. Ultimately, it was concluded that kernels were dominated by the momentum from the discharge compared to the thermal effects of buoyancy.

### 2.2.2. *Temperature Development*

In same study by Sforzo et al. [18], kernel temperatures in a cross-flow were determined between 60 and 200  $\mu\text{s}$  after electrical discharge. Temperature values were primarily determined from the estimated kernel volume, pressure, and deposited energy from the ignition system. The group assumed that the kernel was at a uniform temperature for each time interval. Peak temperatures near 4,000 K were calculated 60  $\mu\text{s}$  after discharge. A rapid decline in kernel temperature was observed until a value of 1,500 K was reached at 150  $\mu\text{s}$ . The rapid temperature decay was attributed to the entrainment of cool surrounding air into the toroidal kernel (as mentioned in section 2.2.1.). Sforzo et al. detected higher intensity (i.e., higher temperature) values from emission images at the downstream location of the kernel within 100  $\mu\text{s}$ . It was stated that the strong vortical motions (induced by the electrode edges) near the electrodes caused increased mixing with the kernel. Although the group was unable to experimentally determine the temperature differences at each side of the kernel, their numerical efforts provided representative temperature values that supported their observations. A maximum temperature difference of roughly 875 K was observed near 100  $\mu\text{s}$ . At 100  $\mu\text{s}$ , the downstream portion of the kernel advected roughly 2.33 electrode diameters downstream while the upstream side was still located near the electrode. Therefore, only the upstream side was susceptible to the increased mixing, which was observed as a decrease in detected emissions. It should be mentioned that representative images indicate that the upstream side of the kernel is loosely attached to the electrodes. This suggests that additional reductions in the kernel emissions could be a result of heat losses to the electrodes, as mentioned by the following groups [28–30].

A numerical study of spark kernels in quiescent nitrogen was simulated by Kono et al. [19]. Conservation of mass, momentum, and energy were used to determine the temperature of kernels. Kernels were discharged from two electrodes under the assumption that heat losses to the electrodes were negligible. The kernel at 50  $\mu\text{s}$  was ellipsoidal, with peak temperatures near 1,000 K. Temperatures decreased to 400 K within a radial distance of 1 mm from the peak temperature. The kernel developed into a torus within 100  $\mu\text{s}$  after discharge, and surrounding fluid was found to flow into the center of the kernel at this time. A peak temperature of 650 K was determined at 100  $\mu\text{s}$ . Temperatures at the edge of the kernel were near 350 K within 0.5 mm of the peak temperature. The temperature difference between the hot core and edge of the kernel was 140 K

along 0.5 mm. These findings are interesting because it suggests that the kernel approaches a more uniform temperature distribution as time progresses.

Further modeling efforts from Ekici et al. [11] used a similar electrode configuration as Sforzo et al. [18], but conducted simulations in quiescent air. Three unique models were used to determine the temperature. The first employed a constant specific heat ratio for dry air. The second utilized simplified equations of state for a diatomic gas. The final method used was originally developed by Capitelli et al. [11], where a large amount of different nitrogen and oxygen species concentrations were analyzed during the spark formation process. According to Ekici et al., all three models resulted in very similar temperature distributions. The peak kernel temperature at 5  $\mu$ s after discharge was over 6,000K. A roughly 4,000K/mm gradient was estimated from the hot center to the cool ambient. Ekici et al. observed an inflow of cold gas into the spark gap within 10  $\mu$ s of discharge, thus preventing the kernel from becoming spherical in shape. Velocity vector fields indicated that a vortex had developed as a consequence of the inflow. A nearly 20 percent decrease in peak temperature was observed between 5 and 10  $\mu$ s because of the heat exchange with the cooler surrounding air.

In another quiescent air study, Blunck et al. [10] determined the temperature of spark kernels using radiation intensity measurements and a deconvolution technique. The technique was based on solving the radiation transfer equation for a non-scattering participating medium [31,32]. The solution to this equation required the path length of the kernel, species concentration, and temperature. The path length was determined by the number of pixels containing a radiation intensity value, and converted to appropriate units of length. Blunck et al. assumed a constant diameter disk such that the number of pixels was equivalent to path length. The concentration of kernels was assumed to be composed of ambient air. A comparison was made between the intensity measurements and solution of the radiation transfer equation. The input temperature was adjusted until the solution of the transfer equation matched the measured radiation intensity. The temperature of kernels typically decreased by 30 percent over 2 cm of spark kernel movement. The vortical structure mentioned in the previous section was found to entrain surrounding air into the center, thereby reducing the temperature at that location. Higher temperatures were observed at the edges of the kernel, supporting the theory that the ring contains the hot gases throughout its lifetime.

### 2.3. Vortex Rings

Numerous studies have observed spark kernels developing into a toroid, often times into a vortex ring. Consequently, literature regarding the fluid mechanics of vortex rings are summarized. The classical work by Maxworthy [33] investigated the structure of laminar vortex rings in a quiescent fluid. A rubber plunger was used to force a column of fluid out of a circular orifice. Dye was placed very near the orifice to visualize the rings. A large amount of dye and vorticity was radially ejected away from the orifice. Surrounding fluid was entrained into the center of the vortex, causing the volume of the ring to increase. This finding was observed by other researchers [34–36] for a uniform diameter under quiescent conditions. Maxworthy [33] mentioned that a considerable amount of dyed fluid was left behind as the vortex ring continued to propagate away from the orifice. He hypothesized that this observation was a consequence of the vortex ring Reynolds number. Nearly 20 years later, Gharib et al. [37] determined that the trailing fluid observed by Maxworthy [33] was dependent on the time needed for vortex rings to reach maximum circulation rather than a Reynolds number dependence. Additional insight from Dabiri [38] stated that any remaining vorticity from the generation of the vortex ring was rejected in the form of a trailing column. This was a consequence of conserving the energy and impulse of vortex rings.

Lim et al. [39] studied vortex rings ejected into a uniform cross-flow for a range of velocities. A significant finding from the group was that the vortex experienced diminished circulation at the upstream side of the ring for all cases. This was a consequence of a reduced relative velocity from the interaction with the cross-flow. Lower circulation suggests that less entrainment was occurring into the vortex ring. Increasing the cross-flow led to additional loss of circulation. Cheng et al. [40] simulated vortex rings in a simple shear flow (i.e., non-uniform cross-flow) using the lattice Boltzmann method (LBM). It is a linear alternative to solving the non-linear Navier-Stokes equations. The computed results highlighted a reduced relative velocity at the upstream side of a vortex ring, similar to Lim et al. [39]. It was determined that the vortex expanded in the shear flow, but the streamwise diameter was larger than the cross-stream. Many insights on vortex rings in a uniform cross-flow were provided by Sau and Mahesh [41]. A decrease in relative velocity at the upstream side was caused by the interaction with the cross-flow, thereby reducing the circulation (effectively the entrainment) at that location. Consequently, the downstream side increased in relative velocity due to mass and momentum conservation. A trailing column of residual vorticity

was detected for vortex rings in a cross-flow under specific stroke ratios, which was directly correlated to the formation number mentioned by Gharib et al. [37]. Iso-surface plots presented by Sau and Mahesh showed that the cross-flow continued around the trailing column rather than being entrained into the vortex itself. This further reduced entrainment of surrounding fluid into the vortex ring.

### 3. Experimental Methodology

The experimental arrangement and approach used to study spark kernels is discussed in this chapter. The setup, data collection method, and technique used to determine kernel temperatures are presented.

#### 3.1. Arrangement

Spark kernels were generated from a Champion Aerospace igniter (CH31627), which is used in gas turbine engines (e.g., Allison T56). The igniter is of the sunken fire configuration [2], and requires 18-24 kV from a compatible exciter (Champion Aerospace, CH305050) to generate kernels. A high voltage ignition lead (Champion Aerospace, CH53399-05) was used to connect the igniter to the exciter. The exciter converted an input electrical signal from a constant voltage source to the designated voltage range. The recommended input range of the exciter was between 10-30 V, yet only 10, 15, and 20 V were considered in this work due to unwanted biasing effects beyond 20 V.

Figure 1 is a representation of the circuit used to determine the supplied energy to spark discharges. A microcontroller (Arduino Uno R3) measured the voltage across a shunt resistor (Vishay Dale  $0.1 \Omega \pm 1\%$ ) during kernel discharge. The sampling rate of the microcontroller was set at 60 Hz (16.67 ms). The microcontroller readings were calibrated with only the shunt and known input voltages, which was then applied to the actual values collected from the igniter circuit in Figure 1. The current was assumed constant throughout the circuit, and was determined using Ohm's Law. Kirchoff's Voltage Law states that the sum of all voltages in a circuit must equal zero. Thus, the voltage across the exciter and igniter combined is estimated to be the difference between the input voltage from the power supply and voltage across the shunt. The energy supplied ( $E$ ) to the igniter was measured by integrating the igniter-exciter voltage ( $V_{DC}$ ) and circuit current ( $I_{DC}$ ):

$$E = \int V_{DC}(t) I_{DC}(t) dt . \quad (1)$$

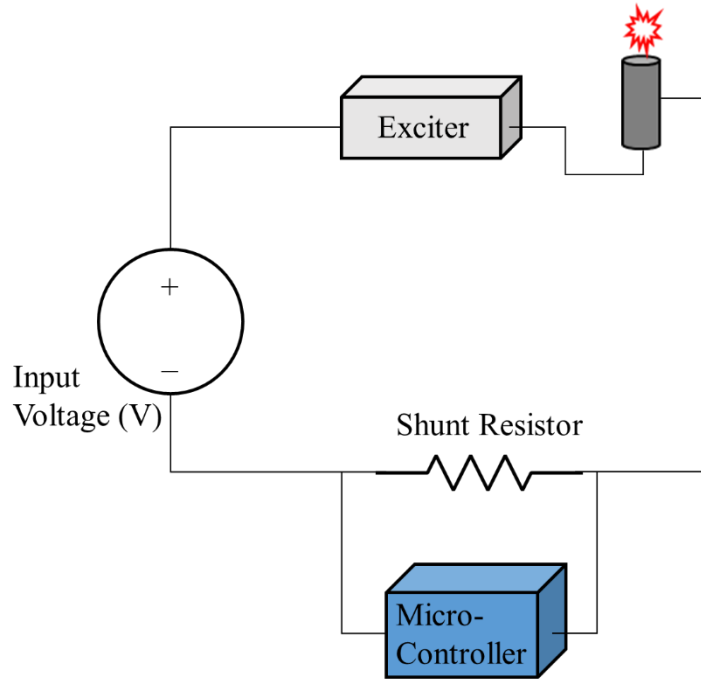


Figure 1: Circuit schematic of igniter to determine supplied energy.

An illustration of the experimental arrangement is shown in Figure 2. The igniter was placed in an open loop, small scale wind tunnel that had a maximum wind speed of 40.2 m/s. The tip of the igniter was positioned 18.4 cm below the top of the wind tunnel and oriented in the downward normal direction. This orientation allowed for the igniter to be placed closer to the center of the test section. Kernel measurements revealed that no statistical difference existed between alternative vertical igniter orientations, which is further discussed in section 4.1.3.

Cross-flow velocities were monitored by measuring the static pressure along the wall of the wind tunnel. Air flow just upstream of the igniter was varied between 5.8-15.6 m/s, with a corresponding Reynolds number of 4,800-12,900 (based on an igniter diameter of 1.28 cm), respectively. A precision velocity meter was inserted into the wind tunnel test section (60.3 cm x 30.5 cm x 29.8 cm) to validate the cross-flow velocity. The velocity from the meter was compared to values determined by the static pressure measurements along the tunnel wall. The velocities agreed within 5-10 percent for the two approaches. The cross-flow velocity ratio, defined as:

$$R_{C.F.} = \frac{V_{jet}}{V_{C.F.}}, \quad (2)$$

is the velocity of the kernel initially ejected ( $V_{jet}$ ) divided by the velocity of the cross-flow ( $V_{C.F.}$ ). Velocity ratios in this work ranged from 0.51-1.38.

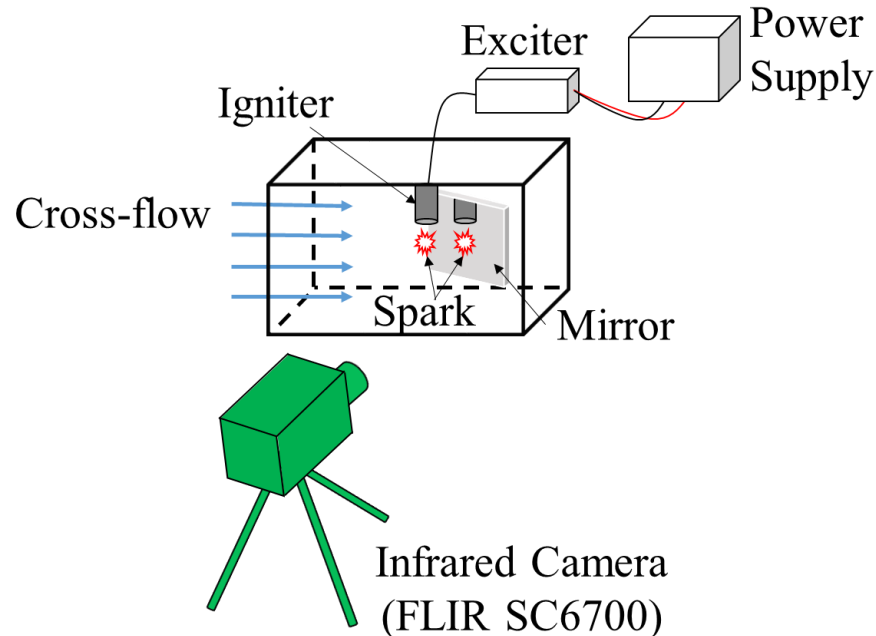


Figure 2: Experimental arrangement for investigating spark discharges into quiescent and cross-flow environments

A mid-wave infrared camera (FLIR SC6700) was positioned perpendicular to the igniter to measure the emitted radiation of kernels after discharge. The camera was placed 1.93 m away from the igniter, resulting in a 1.74 pixel/mm resolution. This was determined by taking a snapshot image of a ruler at the specified distance. The number of pixels within 1 mm was recorded at multiple locations along the ruler and subsequently averaged. This process was performed for a vertical and horizontal ruler orientation, and both resulted in the same resolution.

The infrared camera required optical access to collect radiation emissions from kernels. Initially, a clear plastic film was used to seal one side of the test section. However, it was determined that the radiation emissions using the clear plastic film were uncharacteristically attenuated and scattered, causing discrepancies in the measurements. Ultimately, measurements were collected through a small slot (16.5 cm long, 6.5 cm wide) with no windows to avoid transmission losses.

The additional air which entered through the slot did not influence the trajectory of kernels. Kernel trajectories using the film and with the slot were compared and revealed no significant deviations.

A stainless steel mirror was placed downstream of the igniter to provide a side view of the kernel (see Figure 2). The depth (i.e., path length) of kernels was obtained from this view, which was needed to determine the temperature. Reflected losses of the mirror were calculated to be 15 percent with a blackbody analysis, and were accounted for in the path length information. Smoke visualization was performed to determine a distance where the mirror had limited influence on the flow near the igniter. It was found that a distance of 8 cm between the igniter and mirror was acceptable, as this distance allowed the infrared camera to simultaneously record the reflected and line-of-sight views of the kernel.

### 3.2. Radiation Intensity Measurements

The radiation intensity emitted from the spark kernels was measured using an infrared camera. The camera directly measures photon counts emitted from an object or gas of interest. The camera operates using a 14-bit system, allowing for a dynamic range of 16,384 photon counts per pixel. The integration time of the camera was set to 0.082 ms, with a maximum sampling frequency equal to 1.5 kHz. No more than a 10 percent spatial shift of the kernel was detected with this integration time at the maximum cross-flow velocity. Sample calculations for calculating the integration time with the spatial shift tolerance can be found in Appendix A.

A blackbody calibration was performed at the specified camera-to-igniter distance and integration time to convert the measured photon counts to radiation intensity. A blackbody is an ideal emitter that is used as a calibration source for infrared cameras. Near uniform emissions (in photon counts) are correlated to radiation intensity via the blackbody temperature. Varying the blackbody temperature results in a linear relationship between the photon counts and radiation intensity. The radiation intensity ( $I$ ) is reported as an integrated result:

$$I = \int_{\lambda_j}^{\lambda_k} \alpha_{\lambda} I_{\lambda} d\lambda . \quad (3)$$

Here, the limits of integration are the spectral range of the camera (1-5  $\mu\text{m}$ ), and  $\alpha_{\lambda}$  accounts for the losses through the optics and the spectral response of the camera's detector. The spectral

responses were determined from the data provided by the manufacturers for the listed components (see Appendix B).

Intensity emissions from kernels were captured in the non-linear region of the camera's detector at the specified integration time. Thus, a uniformly hot plate was placed behind the igniter to increase the photon counts to the linear range of the detector response. An additional hot plate was placed outside of the wind tunnel near the inlet, with the hot side facing towards the igniter, to produce the same effect for the reflected image. Intensity emissions from the plate were subtracted from the measurements to determine the intensity of just the kernel. Intensity values below  $0.1 \text{ W/m}^2\cdot\text{sr}$  were not processed because of the low signal-to-noise ratio.

A spark event was considered to be the time from when plasma was formed to the time at which the kernel was no longer detected. Characterizing radiation emissions and temperature of the plasma was not attempted in this work due to detector limits and limitations in solving the radiation transfer equation. Thus, the measurements just following the plasma discharge are reported (0.6-3.3 ms). The kernel development at this time-scale has radiation emissions primarily from carbon dioxide ( $\text{CO}_2$ ) and water vapor ( $\text{H}_2\text{O}$ ) present in the room. It should be mentioned that the time range was established based on the frame rate of the camera. Additionally, the time was determined after plasma was detected and not necessarily at the formation of the plasma. Thus, it is acknowledged that the first image of the kernel does not occur at the same instant in time, rather always 0.6 ms after plasma is detected.

The location of each kernel was determined from an intensity-weighted centroid analysis. The position was calculated in the  $x$  and  $y$  orientations with the following relations:

$$\begin{aligned}\bar{X} &= \frac{\sum I_i x_i}{\sum I} \\ \bar{Y} &= \frac{\sum I_i y_i}{\sum I},\end{aligned}\tag{4}$$

where the subscripts indicate a specific cell location and  $x$  and  $y$  represent the center points of a discrete element relative to a datum.

### 3.3. Deconvolution Technique

The temperature of spark kernels was determined from the radiation intensity measurements using an inverse deconvolution technique and the narrowband radiation model (RADCAL) [32]. The approach used is similar to the work by Blunck et al. [10]. RADCAL is used to solve the radiation transfer equation for a non-scattering participating medium [31,32]:

$$I_{\lambda} = I_{\lambda}(0)\exp(-\tau_{\lambda}) + \int_0^{\tau_{\lambda}} I_{b,\lambda}(\tau_{\lambda}^*)\exp(-\tau_{\lambda} + \tau_{\lambda}^*)d\tau_{\lambda}^*, \quad (5)$$

where

$$\tau_{\lambda} = \int_0^s \kappa_{\lambda} ds, \quad (6)$$

and  $I_{\lambda}(0)$  is an imposed boundary condition. The radiation transfer equation (5) was solved using an initial temperature, chemical composition of air, and path length.

The gases of spark kernels were assumed to be composed of air. The mole fraction of the gases was required for the deconvolution technique, and was determined from measurements and known compositions of air. Carbon dioxide and water vapor concentrations were measured using a coupled CO<sub>2</sub> and humidity device (CO2Meter CM-0018). CO<sub>2</sub> was directly measured in parts per million (ppm). Water vapor concentration was calculated from basic psychrometric equations using the humidity measurements (see Appendix C). Oxygen was assumed constant at 20.95 percent mole fraction, and nitrogen was adjusted accordingly to sum mole fractions of constituents 1 (see Appendix C for further details).

The path length (i.e., depth of kernel) used in the deconvolution technique was determined from reflected images of the kernels. Figure 3 illustrates the process used to determine path lengths. Previous works have approximated kernels as spheres [10,13,42,43], i.e., a series of two-dimensional circles. However, an oval was determined to be a better approximation during kernel development. This allowed the kernel to have a maximum length in either axis or the ability to be approximated as a circle if conditions were appropriate. Thus, kernels were segmented into several

ovals, each with a thickness of  $\Delta h$ . The maximum width and length information from the line-of-sight and reflected images, respectively, were used in the equation of an oval to determine the path

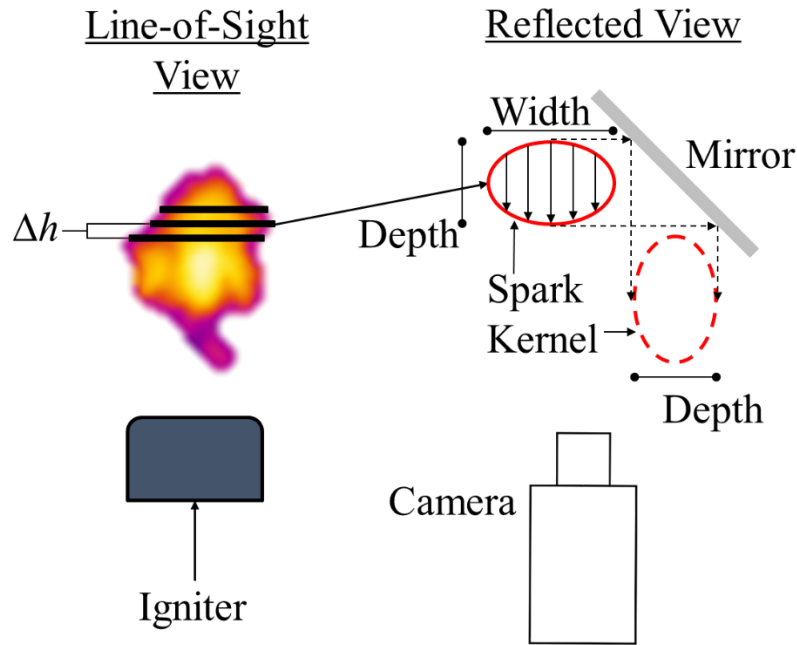


Figure 3: Path length estimate for spark kernels.

length at every pixel where kernels were detected. Both the technique from Blunck et al. [10] and the current work use a uniform and constant temperature (i.e., isothermal) along the path length. This is a limitation using the radiation transfer equation. Thus, reported values should be considered as path-averaged temperatures.

The current work focuses on constructing a database from numerous evaluations of Equation 5, rather than adjusting the temperature until intensities converged with the inverse technique. Essentially, a script was created (see Appendix D) to run a large range of path lengths and initial temperatures to obtain corresponding intensities via Equation 5. In total, 10,000 intensity values were available in the database. A secondary script was used to interpolate the path length and intensity values from the direct measurements to the database (see Appendix E). The output of this procedure was the kernel temperature. It should be mentioned that each database was day-specific (i.e., a unique intensity for different concentrations on different days during data collection). This further improves the accuracy of the technique from repeatability measurements.

Spark kernel temperatures were averaged against a specified tolerance to determine individual temperature contours for quiescent and cross-flow conditions. Temperature distributions were binarized with a one for values greater than 300K and a zero for values below 300K. Binarized contours were summed to a single array. The array contained the number of times a temperature greater than 300K was determined at a specified location. Each value in the array was then compared to the statistically relevant parameter  $n$ :

$$n = \left( \frac{\sigma_{stat}}{SE} \right)^2, \quad (7)$$

where  $SE$  was a user defined tolerance of 10K. The standard deviation ( $\sigma_{stat}$ ) was determined from the temperature distribution. One standard deviation was found to be sufficient for the purposes of determining  $n$ . If a value in the array was equal to or greater than  $n$ , temperatures at that location were averaged across all kernel images. Otherwise, temperatures were not averaged and a value of NaN was assigned. The reasoning behind this process was to encompass kernel variations that were condition specific (i.e., quiescent, cross-flow, phase average, etc.). A constant user defined value for  $n$  was used in previous analyses. However, average kernel temperature contours did not have strong statistical significance using a constant  $n$  with large sample sizes (e.g., greater than 100 spark events).

### 3.4. Evaluation of Technique

#### 3.4.1. Temperature Comparison against Calibration Burner

To evaluate the deconvolution approach, temperature and infrared measurements were collected of a flat flame above a McKenna burner. The burner [44–46] consists of a central porous material (6 cm diameter) through which premixed fuel (ethylene) and air flow. It should be mentioned that the fuel and air in this work was adequately mixed along a length of over 200 tube diameters. Nitrogen flowed through an outer porous region (7.4 outer diameter, 6 cm inner diameter) to protect the flame and reduce entrainment of surrounding air into the flame. The mass flow rate of  $N_2$  was adjusted to match the velocity of the fuel-air mixture to reduce flame instabilities. The McKenna burner was internally cooled with water where the heated liquid was rejected to a sink.

The fuel and N<sub>2</sub> flow rates were controlled with mass flow controllers (MKS M100B and 1179, respectively), and air flow was regulated with a rotameter (Cole Parmer FR4A41BVBN). Prior to producing a flat flame, the controllers and rotameter were calibrated against a bubble Gillibrator to ensure that the proper gas flow rate was received by the burner. The total fuel-air flow rate was held constant at 10,000 SCCM. The equivalence ratios ( $\Phi$ ), defined as:

$$\Phi = \frac{\left( \dot{m}_{fuel} / \dot{m}_{air} \right)}{\left( \dot{m}_{fuel} / \dot{m}_{air} \right)_{stoich}}, \quad (8)$$

ranged from 0.8 to 1.3. Values less than one are considered fuel lean and values greater than unity are fuel rich.

A type-B bare bead thermocouple (OMEGA P30R-008) was inserted into the flame 8.5 mm above the burner surface. This thermocouple has a high temperature range and does not have a Curie point in the anticipated temperature range. This height above the burner allowed measurements to be collected with limited heat loss to the thermocouple and without bias from the burner surface. Additionally, heights near 8.5 mm have been used in previous studies with various techniques [45,47,48]. High temperature ceramic tubing was used to shield the thermocouple wires to reduce interference and noise. A thermocouple reader (OMEGA DPi8-EIT) was used to display the temperature value. This particular reader had an internal cold junction, thus eliminating the need for a lead to be isolated at a known temperature (e.g., submerged in an ice bath). Temperature measurements were collected with the various equivalence ratios and at different radial locations along the burner. Radiation losses were considered in the reported temperatures [49]. Neglecting conduction through the thermocouple, the energy balance was simplified to:

$$\begin{aligned} Q_{conv} &= Q_{rad} \\ h_{conv} A_s (T_f - T_{TC}) &= A_s \sigma \varepsilon (T_{TC}^4 - T_{\infty}^4), \end{aligned} \quad (9)$$

where  $T_f$  is the temperature including radiative losses and  $T_{TC}$  is the temperature reported by the thermocouple. According to Hindasageri et al. [49], the emissivity of a type-B thermocouple can be related to  $T_f$  with the following relation:

$$\varepsilon = (6 \times 10^{-5})T_f + 0.0138 . \quad (10)$$

The only unknown left to solve  $T_f$  is the heat transfer coefficient of the flame ( $h_{conv}$ ). This was calculated from a Nusselt correlation. The appropriate correlation was determined based on the Reynolds number with respect to the thermocouple diameter:

$$\text{Re}_{D_{TC}} = \frac{\rho_f V_{mix} D_{TC}}{\mu_f} , \quad (11)$$

where  $V_{mix}$  represents the fuel-air mixture velocity that flows around the thermocouple of diameter  $D_{TC}$ . The flame properties (e.g., density, viscosity) were assumed to be approximately equal to air, resulting in a Reynolds number less than 0.1. Therefore, the Stokes flow Nusselt correlation mentioned in White [50] was used to estimate  $h_{conv}$ :

$$Nu = 0.42 \text{Pr}^{0.2} + 0.57 \text{Pr}^{1/3} \text{Re}_{D_{TC}}^{0.5} . \quad (12)$$

Equations (9-12) were solved simultaneously to arrive at the corrected temperature.

The temperature determined with the inverse deconvolution technique was found using the approach described in section 3.3. The path length was found from radial thermocouple measurements at a constant height above the burner. The temperature was relatively constant up to a radial distance of 1.5 cm, as seen in Figure 4. Beyond this distance, a rapid decline in the temperature was observed. Note that the width of the flame is less than the central region of the burner because the flame has entrained surrounding air and  $\text{N}_2$  at this height. Considering that the McKenna burner is axisymmetric, the full length at which the temperature was assumed to remain constant was 3 cm. This length was then used in the deconvolution process. Slight variations in

the path length (less than a one percent difference) were detected for different equivalence ratios, but only 3 cm was considered in the deconvolution process.

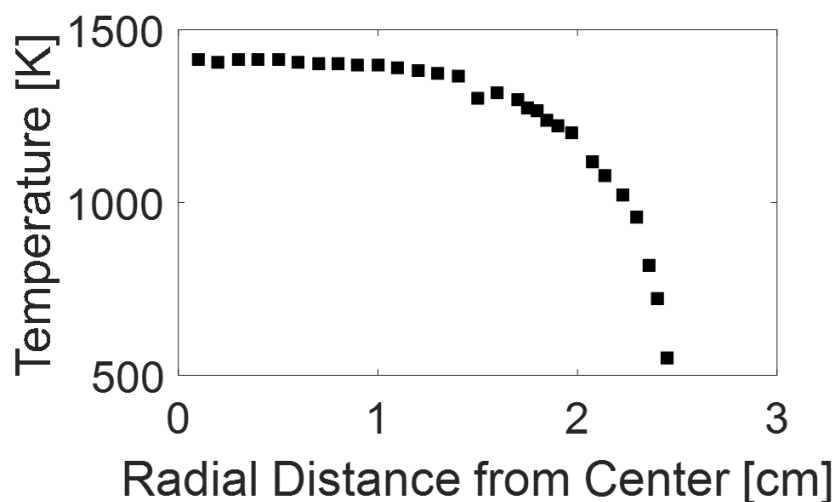


Figure 4: Radial temperature profile of McKenna burner ( $\Phi=1.05$ ).

Calculated (ideal) combustion products used in the deconvolution technique were determined from a program that utilizes the NIST-JANAF thermophysical tables. The mole fraction concentrations of  $\text{CO}_2$ ,  $\text{H}_2\text{O}$ ,  $\text{N}_2$ , and  $\text{O}_2$  for each equivalence ratio were calculated. The concentrations were evaluated at atmospheric pressure and the equivalence ratio specific temperature from the radiation-corrected thermocouple measurements. These values and the estimated isothermal path length for the burner were used in the deconvolution approach to determine temperature.

Figure 5 shows the temperatures obtained from the thermocouple and infrared measurements (inverse deconvolution values). The uncertainty was performed using the Kline-McClintock approach [51]. The relatively large uncertainty in the equivalence ratio was dominated by the resolution of the rotameter used to control the air flow. Thermocouple measurements had less than one percent uncertainty based on manufacturer specifications, thus they have been omitted from Figure 5. Overall, the two measurements agreed within 3-7 percent of each other. The disagreement is attributed to uncertainties in the estimated path length, calculated species concentrations, transmission losses through the optics, and detection limitations of the IR camera.

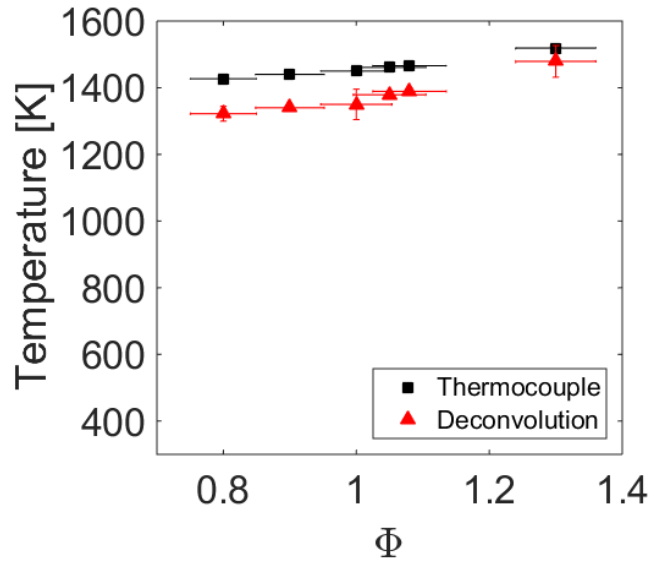


Figure 5: Comparison of thermocouple and deconvoluted temperatures of McKenna burner flame.

### 3.4.2. Sensitivity Analysis

The sensitivity of the deconvoluted temperatures was analyzed for changes in the path length and  $\text{CO}_2$  and  $\text{H}_2\text{O}$  concentrations. The analysis was approached using six random temperature distributions from six different spark events. The variation in temperature between events was less than one percent. In addition to the actual database, supplementary databases were generated with a single variation in either the concentration of  $\text{CO}_2$  or  $\text{H}_2\text{O}$ . The path length was simply adjusted in the script where temperature values were determined. Temperature maps from different times during a spark event were used to ensure the analysis was well represented. The change in temperature was reported as:

$$\Delta T_{SA} = \frac{(T_{adjusted} - T_{actual})}{T_{actual}} \times 100\% . \quad (13)$$

The change in temperature was averaged for each distribution and then subsequently averaged among all the temperature distributions that were selected at random.

Figure 6 shows the results of the sensitivity analysis. A reduction in either concentration by 20 percent led to an increase in deconvoluted temperatures by up to five percent. This is a result of

the absorption coefficient decreasing, thereby requiring a higher temperature to reach a corresponding intensity. Conversely, a 20 percent increase in concentration reduced the temperature by roughly four percent because of increases in the absorption coefficient. Thus, errors in CO<sub>2</sub> or H<sub>2</sub>O concentrations will only yield a relatively small change in the deconvoluted temperature. The path length was the most influential parameter in altering the temperature, with an average temperature change of over 10 percent for a 20 percent reduction in path length. The path length affects the optical thickness. Therefore, decreasing the path length requires a higher temperature to achieve an equivalent intensity, and vice versa.

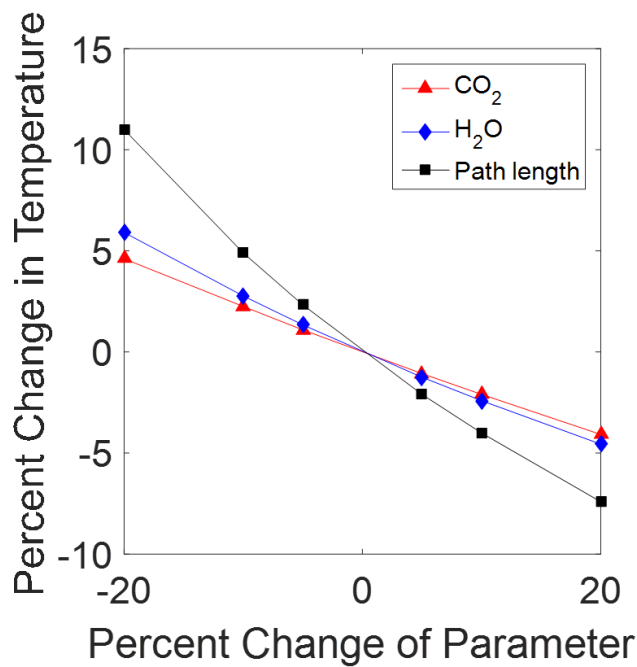


Figure 6: Sensitivity of temperature with variation in key parameters.

### 3.5. Sensible Energy

The sensible energy of spark kernels was estimated to provide a metric for comparing how kernels are influenced by quiescent and cross-flow conditions.

Sensible heat ( $Q$ ) is defined as:

$$Q = mc_p \Delta T, \quad (14)$$

where  $m$  is the mass of an object and  $\Delta T$  is the change in temperature between two processes. According to Law [52], combustion processes that occur in open or unclosed low Mach environments will be influenced more from temporal and spatial effects compared to pressure variations. Thus, spark kernels were evaluated with a constant pressure analysis throughout its evolution. Additionally, no work occurred during this process and changes in kinetic and potential energy were negligible. Therefore, the sensible energy along a path length was derived from Equation (14) to be:

$$U = \frac{PV}{RT} c_p (T - T_\infty), \quad (15)$$

where  $V$  contains the path length and square area visualized by the detector. The sensible energy was integrated across the kernel volume to obtain the total sensible energy.

## 4. Results and Discussion

### 4.1. Quiescent Conditions

Figure 7 shows the radiation intensity emitted by a kernel during a single spark event. The time is relative to when radiation emission from plasma is detected. The spatial coordinates have been non-dimensionalized by the diameter of the igniter. The origin represents the tip of the igniter.

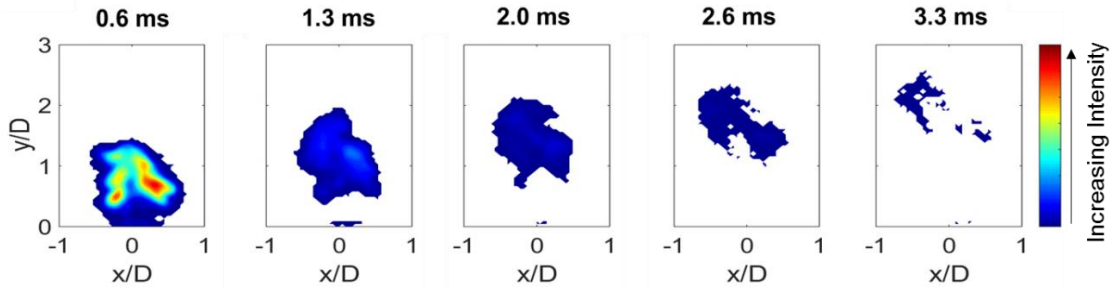


Figure 7: Time resolved emissions from a representative spark kernel.

Spark kernels are approximately oval in shape from a side view, with a width nearly the same diameter as the igniter. Regions of relatively high intensity are evident approximately 0.6 ms after plasma and near the igniter tip. The intensity decreases towards the edges of the kernel as well as with time.

#### 4.1.1. Kernel Development and Bifurcation

The kernels form into a toroidal vortex after leaving the igniter, as evident in images shown in Figure 8. It is seen in the top view images that a void exists at the center of the kernel. This is a consequence of the flow entrainment into the center of the vortex [10,18,19,33,41]. Additional air supplied to the vortex ring from entrainment causes kernels to expand [34–36], as seen in Figure 8. It is postulated that this additional air increases stretching and periodically leads to a separation (or bifurcation) of the kernel. Figure 9 is an illustration of this phenomena for a representative event.

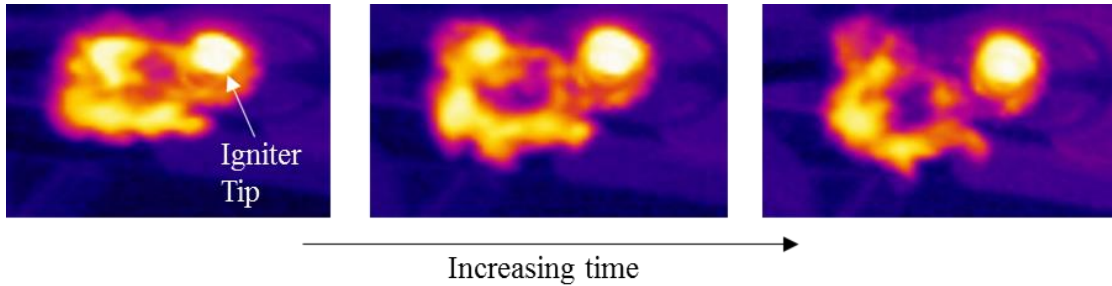


Figure 8: Images of kernel progression into toroidal structure from off axis top view.

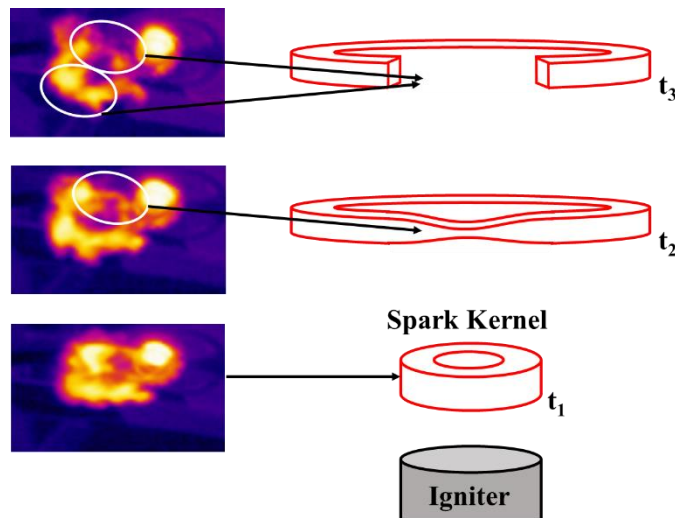


Figure 9: Kernel development leading to bifurcation.

The time between images is designated chronologically with “ $t$ ”. The kernel at  $t_1$  in Figure 9 is right after a spark discharge. Surrounding air has been entrained into the kernel, causing it to expand at  $t_2$ . This would suggest that the strain within the kernel has increased. Note that the kernel in Figure 9 (middle image) experiences thinning at a particular location due to the strain. Continued entrainment into the vortex further increases the strain, which ultimately results in a splitting at  $t_3$ . Roughly one-third of all spark events result in a bifurcation (i.e., splitting at two locations), based on analysis of more than 700 spark discharges. This observation was not influenced by the flow condition (i.e., quiescent, cross-flow). Kernels that did not bifurcate continued to develop and propagate until radiation emissions were no longer detected.

Additional evidence for kernels developing into a vortex ring is evident in Figure 10, where a trailing column [33,37,38,53–56] of hot gas has been detected. The creation of the trailing column

is a result of reaching the critical formation number of a vortex ring [37,38]. The critical formation number is a non-dimensional time at which vortex ring has reached maximum circulation [37,38,54]. Consequently, the ring cannot accept remaining vorticity left over from its formation [33,38]. It is hypothesized that this excess vorticity is rejected as a trailing shear layer (i.e., trailing column) [38]. In this case, the trailing shear layer would be heated fluid that was initially exchanged with the ring's hot gases. Readers are referred to References [37] and [38] for further details regarding the formation number of vortex rings and its implications. Similar observations relating to the kernel's entrainment, expansion, and trailing column have been documented for kernels discharged using a pulsed plasma jet igniter [10], a laser [9], and dielectric gap [11,18,19].

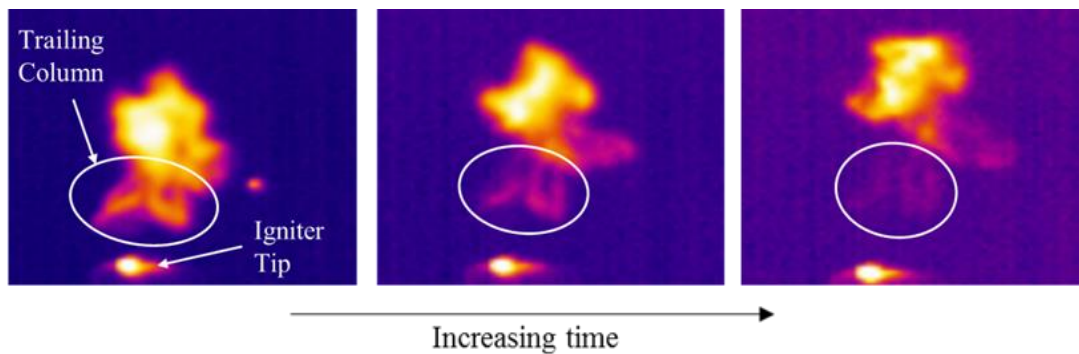


Figure 10: Line-of-sight images showing trailing column from kernel development.

#### 4.1.2. Voltage Dependence

The exciter has the ability to operate under variable input voltages. A comparison between supply energy, input voltage, and sensible energy was made to determine if an influence existed.

Three voltages were evaluated and the energy supplied was calculated. The average energy supplied was nearly 10 J for all three cases. An equivalent supplied energy ( $E$ ) would equate to similar kernel temperatures assuming that  $E$  was equivalent to sensible energy ( $U$ ) in Equation (15), *ceteris paribus*. Comparison of the average spark kernel temperatures and spatial distributions of each voltage differed by less four percent in this work. Although the kernel temperatures are not discussed, the overall trends are still valid and applicable.

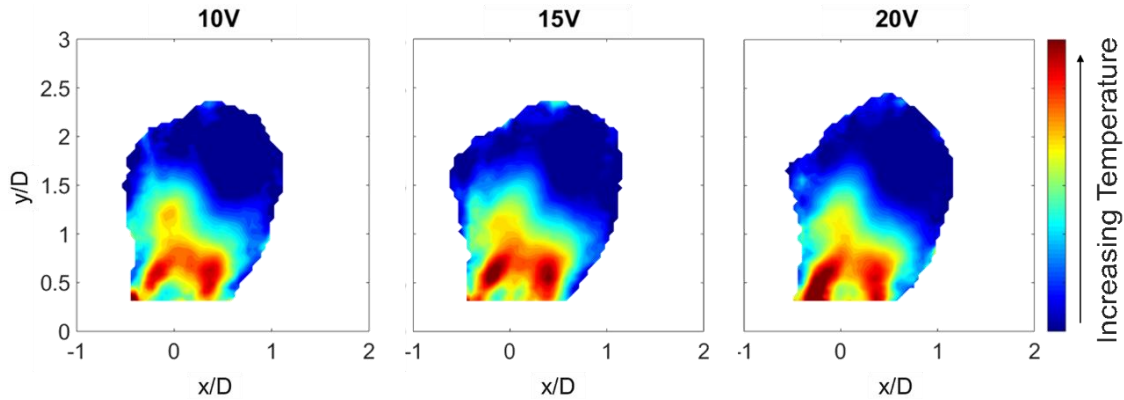


Figure 11: Average kernel temperatures from roughly 100 spark events.

In lieu of the voltage insensitivity, the remainder of the results presented in this section will be for an input voltage of 15 V. It is important to note, however, that increasing the voltage resulted in more frequent discharges. Thus, it is possible to deliver more power to the system by generating additional kernels. This could be advantageous depending on the demand or operating conditions.

#### 4.1.3. Temperature Results

The spatial and temporal temperature evolution of over 400 spark events with a 15 V power supply were averaged in a quiescent environment. Phase averaged results are shown in Figure 12.

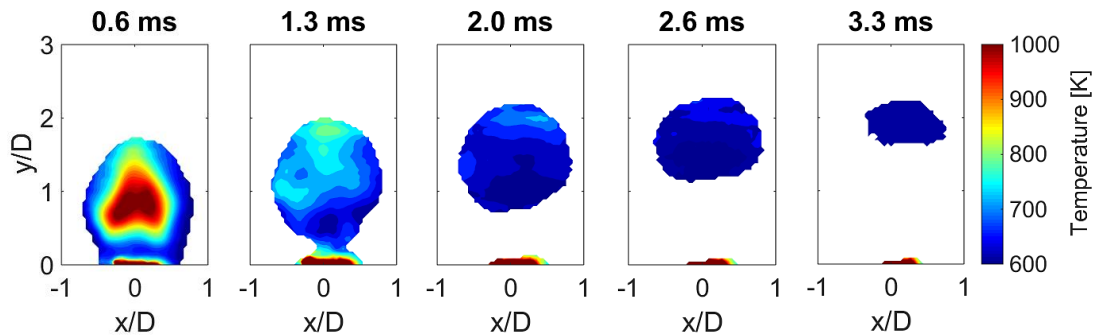


Figure 12: Phase averaged kernel temperatures

A region of high temperatures was observed near the center 0.6 ms after detecting plasma. Observations of individual images at this time show a jet-like structure for the kernel, which suggests that the gases were ejected with relatively high temperature and high momentum from the igniter tip. Similar observations made by Maxworthy [33] for vortex rings state that a large amount of fluid ejected axially away during the production of the ring. Additionally, Kono et al.

[19] numerically determined that the hot kernel traveled at a high velocity outward soon after discharge. Average peak temperatures at 0.6 ms were near 1200 K. After 1.3 ms, peak temperatures (~810 K) were observed near the top half of the kernel. The lower temperatures in the bottom half were attributed to the trailing column of the kernel (i.e., Figure 10); the top half was the main portion of the kernel. Relatively cool surrounding air was entrained from the bottom of the kernel through to the center. Hot gases in the ring exchanged heat with the newly introduced air, resulting in an overall decrease in kernel temperature. The temperature distribution of kernels beyond 2 ms was approximately uniform. Similar observations were reported by Kono et al. [19], yet for different time scales. Some low temperatures of the kernel were not captured due to detection limits with the IR camera. This resulted in a decreased apparent size of the kernel. The temperatures continued to decrease throughout the kernel's lifetime, even beyond 3.3 ms.

The time averaged kernel temperatures are seen in Figure 13. Peak values near 950 K were determined within one diameter from the igniter tip. This value is lower compared to the phase results due to an averaging shift past two locations. Note that the peak temperature is not located at the igniter tip because measurements of the plasma and kernel just lifting from the igniter have been neglected because of limitations in the deconvolution technique. The main influence of the vortex ring is evident in this figure; two symmetric hot regions are seen near the edges of the kernel (yellow and red) and a relatively cooler region in the center was apparent near  $y/D = 0.5$ . The cooler temperatures at the center were a result of the path averaged temperatures as well as the toroid itself; hot gases are not present at the center core. As mentioned earlier, the technique assumes a single path length of uniform temperature through the kernel, whereas the toroid shape suggests temperature variations. Thus, a larger length with the same intensity would yield a lower temperature. Challenges in determining the dimensions of the vortex rings as they develop hinder improving the deconvolution approach to avoid assuming isothermal path lengths.

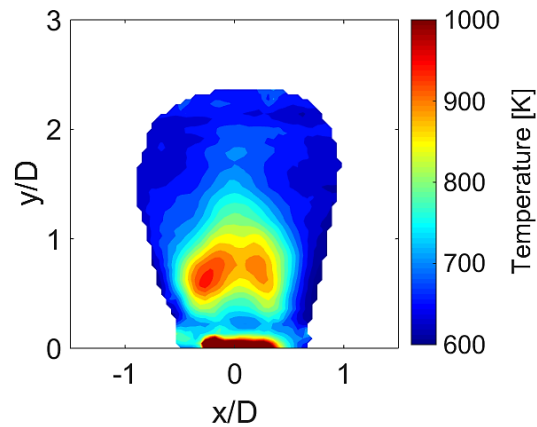


Figure 13: Average temperature of kernels in a quiescent environment

It is worth mentioning that the diameter of the kernel shown in Figure 13 at  $y/D = 0.6$  is near  $1.3D$ . Bond and Johari [35] observed a vortex ring diameter of approximately  $1.4D$  at the same vertical height. This comparison further supports that kernels develop into a toroidal vortex.

Measurements were collected with the igniter orientated in two directions to assess the effect of buoyancy. The igniter was discharged with the tip facing upward and downward (relative to gravity). The average temperature values and spatial distribution for the two orientations were compared and the values typically agreed within six percent, suggesting that buoyancy effects were negligible. Similar findings were reported by Blunck et al. [10] for a pulsed plasma-jet igniter.

#### 4.1.4. Trajectory

A spark kernel's location was determined based on the approximate centroid from the radiation intensity measurements. Detected kernels are shown as symbols in Figure 14, where the red dashed lines represent the region where 95 percent of kernels were detected. The trajectory of kernels under quiescent conditions tended to be vertical, nearly symmetric, with a maximum spread of roughly two igniter diameters at  $y/D = 2$ . A portion of these centroids are material ablating off the igniter (i.e., not kernels). While evident in analyzing the trajectories, sparks did not alter the reported temperature values because of precautions in the data reduction. It should be noted that results presented in this work are for a specific igniter orientation. Extended use of the igniter tended to cause the kernels to favor certain trajectories. A slightly higher concentration of kernels

are detected to the right of the origin in Figure 14. However, this did not directly affect the resulting kernel temperature.

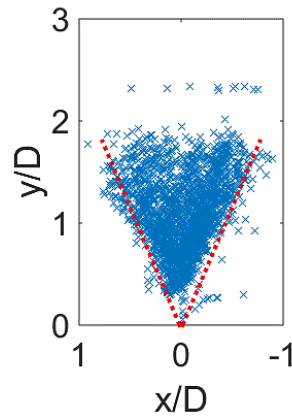


Figure 14: Trajectory of kernels in a quiescent environment

The average velocity of kernels was determined from the trajectory information and sampling frequency of the camera (Figure 15). The average kernel velocity was 8 m/s at 0.6ms and was evaluated at a height of  $y/D = 0.73$ . This was determined to be the average minimum height above the igniter after the plasma was fully dissipated and when the kernel was initially detected. The error bars were determined using the standard deviation and sample size of the calculated velocities with 95 percent statistical significance. The velocity exhibited an exponential decay for the remaining time shown in Figure 15. The velocity information was used to determine the cross-flow velocity ratio used later in this effort.

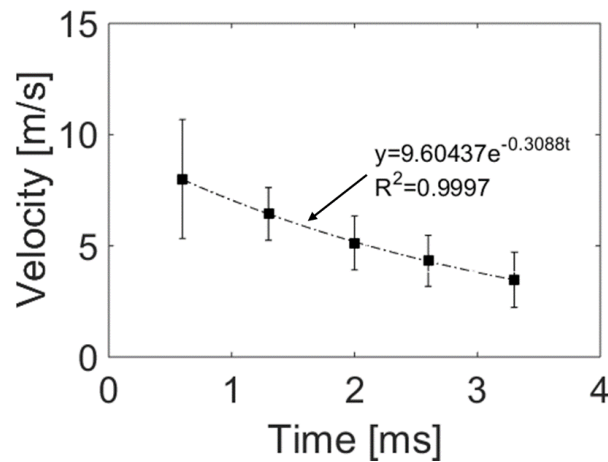


Figure 15: Kernel velocity in a quiescent environment

## 4.2. Cross flow Conditions

### 4.2.1. Kernel Development

Spark kernels were discharged in a uniform cross-flow and the spatial and temporal development of kernels was determined. Radiation intensity of kernels in a cross-flow (see Figure 16) are roughly oval in shape. The intensity distribution at the lowest cross-flow velocity (top panel) and 0.6 ms after discharge is similar to the kernel in quiescent conditions. A region of high intensity is centrally located with relatively lower intensity values at the edges. However, a stark contrast can be seen at the highest cross-flow velocity (bottom panel), where higher intensity is located at the upstream side of the kernel. The reasoning behind this observation will be discussed further in this section. The apparent size of the kernel decreases with time, as the intensity decreases below infrared detection from the camera.

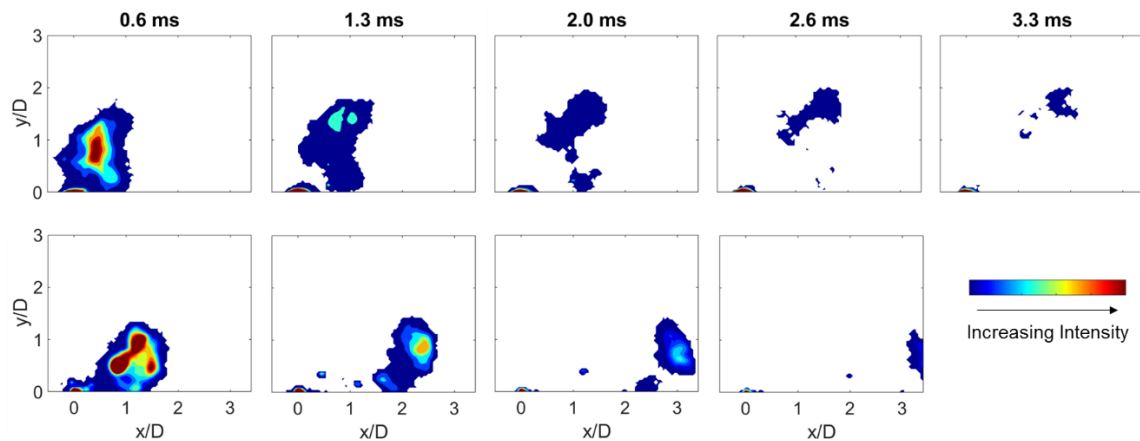


Figure 16: Raw instantaneous intensity of kernels in a 5.8 m/s (top) and 15.6 m/s (bottom) cross-flow.

A reduction in vertical penetration and increased downstream propagation per time is observed for kernels in a cross-flow compared to kernels discharged in quiescent conditions. This suggests that the cross-flow momentum is larger than the ejection momentum of the kernel. These observations agree with the cross-flow velocity ratio values determined in Section 3. The ratio is essentially the relationship between kernel and cross-flow momentums. It was assumed that the density of the kernel and cross-flow were equal in this work. As mentioned earlier, buoyant forces were determined to be negligible. Therefore, density differences between elevated and ambient temperatures was negligible as well. Thus, cross-flow velocity ratios less than unity would indicate lower fluid momentum of the ejected kernel compared to the cross-flow momentum. Increasing

the cross-flow velocity resulted in even further downstream propagation and decreased vertical propagation.

#### 4.2.2. Temperature Results

Figure 17 shows the phase averaged temperature results for the three cross-flow conditions. The temperature distribution within the kernels are generally similar to those for quiescent conditions. Peak temperatures are observed at the center of the kernel, followed by a decrease in temperature with time until the kernel is no longer detected. Note, however, higher average peak temperatures occur after 0.6 ms in a cross-flow (up to 1300 K) compared to 1200 K in quiescent conditions for the same time. Sforzo et al. [18] reported temperatures near 1400 K after 0.2 ms from discharge in a 33 m/s cross-flow. Note that kernels exhibit an anti-symmetric temperature distribution, where noticeably higher temperatures are located at the upstream side of the kernel compared to the downstream. Average kernel temperatures decay more rapidly with increases in the cross-flow velocity between 0.6 and 1.3 ms. For example, kernels discharged in the lowest cross-flow decreased by roughly 325 K compared to approximately 500 K at the highest cross-flow. This was attributed to the increased surface area due to elongation of the kernel, which, in turn, increased the heat transfer by the cross-flow.

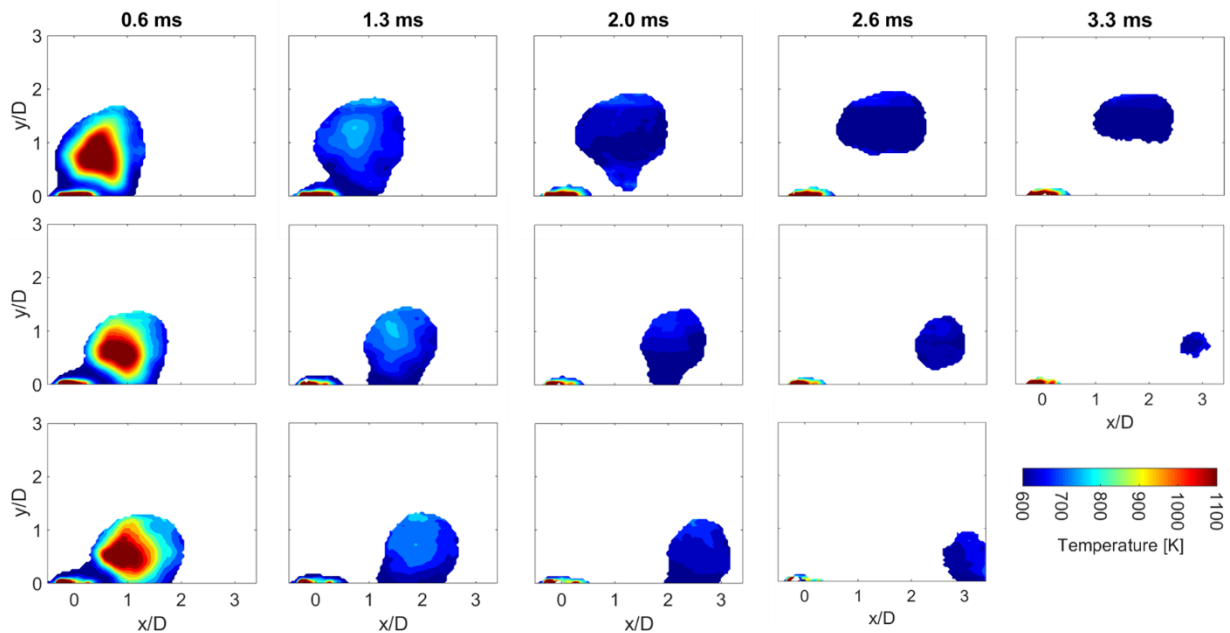


Figure 17: Phase averaged kernels in a cross-flow velocity of 5.8 m/s (top), 11.2 m/s (middle), and 15.6 m/s (bottom). Flow is left to right.

The sensitivity of kernel temperature to different cross-flow velocities is caused by changes in entrainment into the vortex. Figure 18 is a representation of the interactions of the velocity fields of the vortex and cross-flow. The relative velocity at the top of the vortex is reduced on the upstream side [39]. This tends to decrease the entrainment into the vortex because of the reduced vorticity. Interestingly, the bottom of the kernel does not experience an increased relative velocity, as would be expected because of the interaction of the vortex and cross-flow velocity fields. The cross-flow continues in the streamwise direction around the trailing column [41] located at the bottom of the vortex ring (see Figure 10). This inhibits further entrainment of surrounding air [41] at the upstream side of the kernel resulting in higher temperatures relative to the downstream. The downstream portion of the vortex ring, on the other hand, had greater entrainment in a cross-flow [40,41]. This is due to the conservations of angular momentum and circulation [55,57], and thus, the kernel will entrain additional air at the downstream side of the kernel. The cooler air will decrease the kernel temperature due to the heat exchange with a greater heat transfer coefficient.

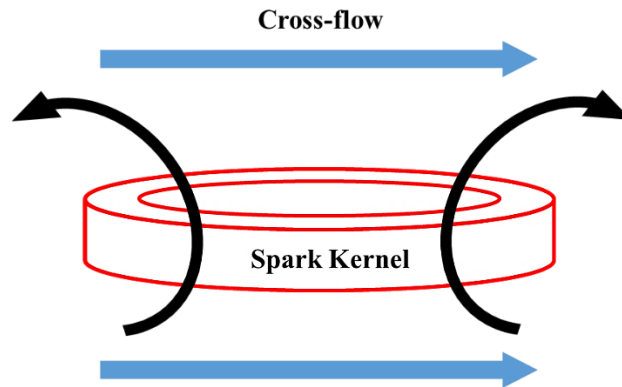


Figure 18: Illustration of kernel interaction with cross-flow.

The average temperatures of spark kernels are shown in Figure 19. The location of peak kernel temperatures exhibit a dependence on the cross-flow velocity. The lowest cross-flow velocity (left panel) indicates peak values ( $\sim 1050$  K) are near  $x/D = 0.33D$  downstream. Recall that data collected just as the kernels lift from the igniter are not processed, hence the peak temperatures are not next to the igniter. Doubling the velocity (middle panel) resulted in twice the downstream propagation with a peak temperature of 1120 K. The increase in temperature occurs because the cross-flow reduces entrainment into the toroidal vortex. A similar relationship was observed between the 9,600 and 12,900 Reynolds number conditions; a roughly one-third diameter increase

in streamwise propagation for an equivalent increase in velocity. The maximum average temperature was near 1250 K for a cross-flow velocity of 15.6 m/s.

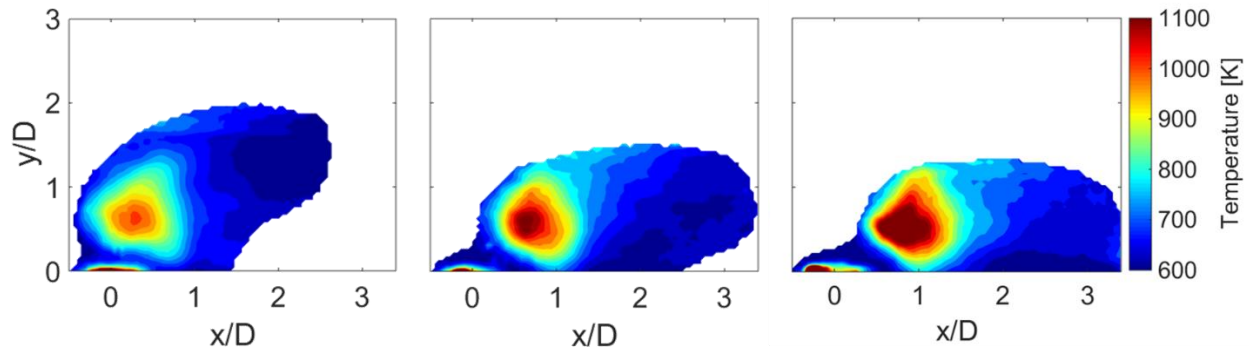


Figure 19: Average temperatures for kernels in 5.8 m/s (left), 11.2 m/s (middle), and 15.6 m/s (right) cross-flow velocity.

#### 4.2.3. Trajectory

The trajectory of kernels for different cross-flow conditions is shown in Figure 20. The solid black curve represents the average trajectory and the dashed red lines encompass 95 percent of kernels detected. All three cases are well matched with a polynomial fit. It is important to reiterate that the igniter is not flush with the wind tunnel wall. Previous work has observed large wall effects on the vortex ring development and entrainment [41,58,59].

A majority of kernels at the lowest cross-flow velocity (left panel) were detected at half a diameter downstream. The intermediate cross-flow velocity (middle panel) was twice as large and resulted in a kernels being detected nearly twice as far downstream. A 33 percent increase in the spread (i.e., distance between dashed red lines) of detected kernels was observed at the highest cross-flow velocity. This was attributed to the instability and susceptibility of kernels to the flow structures at that velocity.

The trajectory of a pulsed jet from an elevated nozzle [60] was compared to detected kernels in comparable cross-flow velocity ratios ( $R_{C.F.}$ ). At the lowest cross-flow (left panel), the trajectories of kernels and pulsed jets was not well matched despite a less than 10 percent difference between the two ratios. However, the pulsed jet trajectory at half the ratio was very similar to the path of kernels. The same occurrence was observed for the intermediate and highest cross-flow velocities (middle and right panels, respectively), where pulsed jets with half the cross-flow ratio matched

the trajectory of kernels. It is hypothesized that the initial velocity of kernels discharged from the igniter was twice as large as originally determined. Due to plasma saturating the detector of the IR camera, the initial centroid location of the kernel could not be determined.

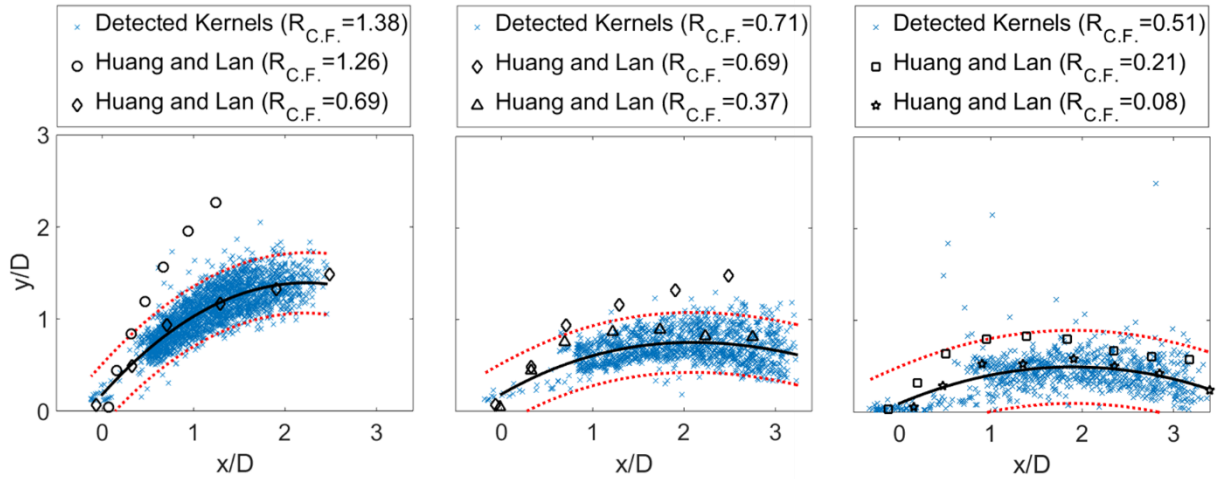


Figure 20: Kernel trajectory compared against an elevated pulsed jet for 5.8 m/s (left), 11.2 m/s (middle), and 15.6 m/s (right) cross-flow velocities.

#### 4.2.4. Sensible Energy Results

Sensible energy results seen in Figure 21 indicate that kernels in a higher cross-flow contain less sensible energy per time compared to quiescent and low cross-flow conditions. The apparent kernel volume decreases in the presence of a cross-flow even though higher temperatures were determined. Only spark kernels in the 11.2-15.6 m/s cross-flow range were statistically variant, where kernels in the 5.8 m/s environment were similar to quiescent conditions.

The large difference between the supplied energy (10 J) and sensible energy is attributed to the radiative losses and convective and conductive heat losses to the electrodes [8]. According to Zeldovich [61], the efficiency of a spark ignition system is between 2-16 percent, which was defined as the ratio between the energy of a spherical volume to the supplied electrical energy. The approach assumes an initial temperature of the spherical volume, whereas this work has quantified the temperature. Theoretically, the maximum efficiency for this current work would be between 6-7.5 percent using the sensible energy of the kernel at 0.6 ms. However, the relationship defined by Zeldovich is only for a reacting flow. Thus, a direct comparison is not necessarily valid, but a

value determined within the range specified by Zeldovich under non-reacting conditions is intriguing.

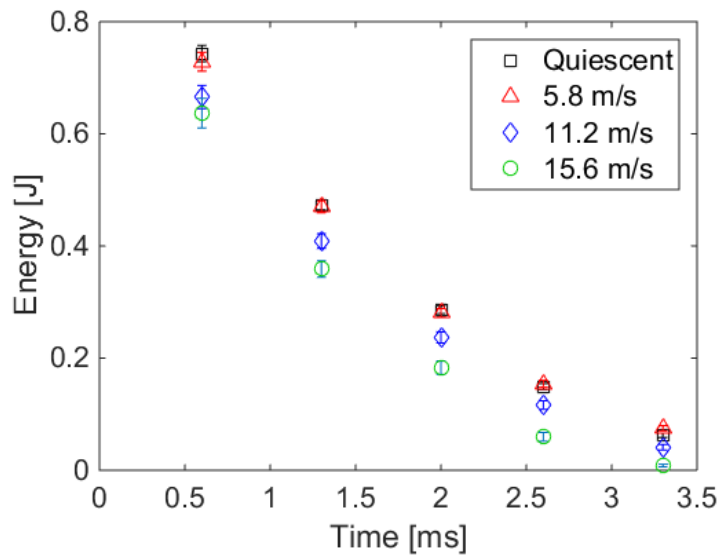


Figure 21: Sensible energy of spark kernels for quiescent and cross-flow conditions

## 5. Summary and Conclusions

In summary, line-of-sight radiation intensity measurements of spark kernels were collected using an infrared camera. Kernels were discharged from a gas turbine engine igniter under quiescent and cross-flow conditions. The spread and trajectory of kernels were determined for a quiescent environment and a range of cross-flow velocities. The temperature of kernels was determined from a deconvolution technique that incorporated the intensity measurements and solution of the radiation transfer equation of a non-scattering participating medium. Temperature of the initial plasma was not considered due to limitations in solving the radiation transfer equation. Only the successive temperatures after plasma were reported. The technique was evaluated using a well characterized laminar flame and assessed by a sensitivity analysis using kernel temperature distributions. The supplied energy to kernels was determined using voltage measurements collected from a microcontroller connected to the ignition system. The sensible energy was determined from the deconvoluted temperatures and spatial information of kernels.

Using these measurements, the conclusions from this effort are as follows:

- I. Spark kernels develop into a vortex ring. A high momentum jet of hot gas is ejected from the igniter tip after plasma discharge. The induced shear between the jet and surroundings creates vorticity that leads to entrainment into the vortex. A column of fluid trails behind the kernel as a result of rejecting additional vorticity after the vortex ring reaches maximum circulation.
- II. Kernels propagate vertically under quiescent conditions. A maximum spread of two igniter diameters was observed in the infrared. The distribution of detected kernels is nearly symmetric.
- III. Average peak kernel temperatures in a quiescent environment reach up to 950 K within half an igniter diameter in the vertical direction and within 0.6 ms after detecting plasma.
- IV. Average peak temperatures in a cross-flow occur within 0.6 ms after detecting plasma. Values ranged from 1050-1250 K for cross-flow velocities between 5.8-15.6 m/s, respectively.
- V. Interaction between the kernel and cross-flow results in decreased entrainment and increased temperature, particularly on the upstream side. The relative velocity at the top of

the vortex decreases on the upstream side. The bottom of vortex at the upstream side is not affected because the trailing column of fluid inhibits the cross-flow into the ring. The decrease in entrainment results in elevated temperatures compared to values determined for quiescent conditions. Increases in the cross-flow velocity further reduced the entrainment, producing higher temperatures.

- VI. Kernel trajectories in a cross-flow experience decreased vertical penetration, but increased streamwise propagation. The trajectory was well matched with literature from a pulsed jet, yet at half the determined cross-flow ratio. Limitations in determining the initial kernel's centroid were thought to cause the discrepancy.
- VII. Bifurcation of the kernel is detected for one-third of all spark events, independent of ambient conditions (i.e., quiescent, cross-flow). Expansion of the kernel, due to entrainment of surrounding air, leads to increased strain. This strain can cause splitting of the kernel.
- VIII. The sensible energy of kernels at the lowest cross-flow velocity is comparable with the energy determined under quiescent conditions. Increasing the cross-flow results in less sensible energy per time. This observation is attributed to an apparent reduction in the kernel's size as a consequence of infrared detection capabilities.

## References

- [1] T.M. Muruganandam, S. Nair, D. Scarborough, Y. Neumeier, J. Jagoda, T. Lieuwen, et al., Active Control of Lean Blowout for Turbine Engine Combustors, *J. Propuls. Power.* 21 (2005) 807–814. doi:10.2514/1.7254.
- [2] A. Lefebvre, D. Ballal, *Gas Turbine Combustion: Alternative Fuels and Emissions*, Third, CRC Press, Boca Raton, 2010.
- [3] J. Hilliard, G. Springer, *Fuel Economy in Road Vehicles Powered by Spark Ignition Engines*, 1st ed., Plenum Press, New York, 1984.
- [4] R.K. Eckhoff, M. Ngo, W. Olsen, On the minimum ignition energy (MIE) for propane/air., *J. Hazard. Mater.* 175 (2010) 293–7. doi:10.1016/j.jhazmat.2009.09.162.
- [5] T.-W. Lee, V. Jain, S. Kozola, Measurements of minimum ignition energy by using laser sparks for hydrocarbon fuels in air: propane, dodecane, and jet-A fuel, *Combust. Flame.* 125 (2001) 1320–1328. doi:10.1016/S0010-2180(01)00248-6.
- [6] S.P.M. Bane, J.L. Ziegler, P.A. Boettcher, S.A. Coronel, J.E. Shepherd, Experimental Investigation of Spark Ignition Energy in Kerosene , Hexane , and Hydrogen, *J. Loss Prev. Process Ind.* 26 (2013) 290–294.
- [7] National Advisory Committee for Aeronautics Report 1300-Basic Considerations in the Combustion of Hydrocarbon Fuels with Air, 1959.
- [8] I. Glassman, *Combustion*, Third, Academic Press, San Diego, 1996.
- [9] S.S. Harilal, B.E. Brumfield, M.C. Phillips, Lifecycle of laser-produced air sparks, *Phys. Plasmas.* 22 (2015) 063301. doi:10.1063/1.4922076.
- [10] D. Blunck, B. Kiel, L. Goss, A. Lynch, Spatial Development and Temperature of Spark Kernels Exiting into Quiescent Air, *J. Propuls. Power.* 28 (2012) 458–465.

- [11] O. Ekici, O. a. Ezekoye, M.J. Hall, R.D. Matthews, Thermal and Flow Fields Modeling of Fast Spark Discharges in Air, *J. Fluids Eng.* 129 (2007) 55. doi:10.1115/1.2375130.
- [12] K. Eisazadeh-Far, F. Parsinejad, H. Metghalchi, J.C. Keck, On flame kernel formation and propagation in premixed gases, *Combust. Flame.* 157 (2010) 2211–2221. doi:10.1016/j.combustflame.2010.07.016.
- [13] S. Barbosa, P. Scouflaire, S. Ducruix, G. Gaborel, Comparisons Between Spark Plug and Laser Ignition in a Gas Turbine Combustor, in: *Eur. Combust. Meet., Chania, 2007*: pp. 1–6.
- [14] N.R. Grady, R.W. Pitz, S. Menon, B. Ochs, T. Slais, J. Berlette, et al., OH PLIF Laser Diagnostics of Turbulent, Compressible, Premixed, Freely Propagating Flame Kernels, in: *52nd Aerosp. Sci. Meet., American Institute of Aeronautics and Astronautics, Reston, Virginia, 2014*: pp. 13–17. doi:10.2514/6.2014-0315.
- [15] T.M. Ombrello, C.D. Carter, C.-J. Tam, K.-Y. Hsu, Cavity ignition in supersonic flow by spark discharge and pulse detonation, *Proc. Combust. Inst.* (2014) 1–8. doi:10.1016/j.proci.2014.07.068.
- [16] M.W. Peng, S. (Steven) Shy, Y.W. Shiu, C.C. Liu, High pressure ignition kernel development and minimum ignition energy measurements in different regimes of premixed turbulent combustion, *Combust. Flame.* 160 (2013) 1755–1766. doi:10.1016/j.combustflame.2013.03.030.
- [17] T.C. Lieuwen, V. Yang, *Gas Turbine Emissions, First*, Cambridge University Press, New York, 2013.
- [18] B. Sforzo, A. Lambert, J. Kim, J. Jagoda, S. Menon, J. Seitzman, Post discharge evolution of a spark igniter kernel, *Combust. Flame.* 162 (2015) 181–190. doi:10.1016/j.combustflame.2014.07.024.

- [19] M. Kono, K. Niu, T. Tsukamoto, Y. Ujiie, Mechanism of Flame Kernel Formation Produced by Short Duration Sparks, in: Twenty-Second Symp. Combust., Seattle, 1988: pp. 1643–1649.
- [20] S. Blakey, L. Rye, C.W. Wilson, Aviation gas turbine alternative fuels: A review, Proc. Combust. Inst. 33 (2011) 2863–2885. doi:10.1016/j.proci.2010.09.011.
- [21] F.A. Williams, Combustion Theory, 2nd ed., 1985.
- [22] T. Lieuwen, Unsteady Combustor Physics, Cambridge University Press, 2012.
- [23] B. Coudour, K. Chetehouna, S. Rudz, P. Gillard, J.P. Garo, Investigation on minimum ignition energy of mixtures of  $\alpha$ -pinene–benzene/air, J. Hazard. Mater. 283 (2015) 507–511. doi:10.1016/j.jhazmat.2014.09.057.
- [24] V. Tihay, P. Gillard, D. Blanc, Ignition study of acetone/air mixtures by using laser-induced spark., J. Hazard. Mater. 209-210 (2012) 372–8. doi:10.1016/j.jhazmat.2012.01.040.
- [25] S. Kondo, A. Takahashi, K. Tokuhashi, Calculation of minimum ignition energy of premixed gases, J. Hazard. Mater. 103 (2003) 11–23. doi:10.1016/S0304-3894(03)00226-7.
- [26] B. Lewis, G. von Elbe, Combustion, Flames, and Explosions of Gases, Third, Academic Press, Orlando, 1987.
- [27] W. Jost, Explosion and Combustion Processes in Gases, First, McGraw Hill, New York, 1946.
- [28] D.A. Eichenberger, W.L. Roberts, Effect of Unsteady Stretch on Spark-Ignited Flame Kernel Survival, Combust. Flame. 118 (1999) 467–478.

- [29] J. Han, H. Yamashita, N. Hayashi, Numerical study on the spark ignition characteristics of a methane–air mixture using detailed chemical kinetics, *Combust. Flame*. 157 (2010) 1414–1421. doi:10.1016/j.combustflame.2010.02.021.
- [30] F. Tholin, D. a. Lacoste, A. Bourdon, Influence of fast-heating processes and O atom production by a nanosecond spark discharge on the ignition of a lean –air premixed flame, *Combust. Flame*. 161 (2014) 1235–1246. doi:10.1016/j.combustflame.2013.11.007.
- [31] M.F. Modest, *Radiative Heat Transfer*, First, McGraw Hill, New York, 1993.
- [32] W. Grosshandler, *RADCAL: A Narrow-Band Model for Radiation Calculations in a Combustion Environment*, Washington, D.C., 1993.
- [33] T. Maxworthy, The structure and stability of vortex rings, *J. Fluid Mech.* 51 (1972) 15–33.
- [34] a. Weigand, M. Gharib, On the evolution of laminar vortex rings, *Exp. Fluids*. 22 (1997) 447–457. doi:10.1007/s003480050071.
- [35] D. Bond, H. Johari, Impact of buoyancy on vortex ring development in the near field, *Exp. Fluids*. 48 (2009) 737–745. doi:10.1007/s00348-009-0761-z.
- [36] A. Borghese, A. D’Alessio, M. Diana, C. Venitozzi, Development of Hot Nitrogen Kernel, Produced by a Very Fast Spark Discharge, in: *Twenty-Second Symp. Combust.*, Seattle, 1988: pp. 1651–1659.
- [37] M. Gharib, E. Rambod, K. Shariff, A universal time scale for vortex ring formation, *J. Fluid Mech.* 360 (1998) 121–140.
- [38] J.O. Dabiri, Optimal Vortex Formation as a Unifying Principle in Biological Propulsion, *Annu. Rev. Fluid Mech.* 41 (2009) 17–33. doi:10.1146/annurev.fluid.010908.165232.
- [39] T.T. Lim, K.B. Lua, K. Thet, Does Kutta lift exist on a vortex ring in a uniform cross flow?, *Phys. Fluids*. 20 (2008) 051701. doi:10.1063/1.2911709.

- [40] M. Cheng, J. Lou, T.T. Lim, Motion of a vortex ring in a simple shear flow, *Phys. Fluids*. 21 (2009) 10–14. doi:10.1063/1.3196903.
- [41] R. Sau, K. Mahesh, Dynamics and mixing of vortex rings in crossflow, *J. Fluid Mech.* 604 (2008) 389–409. doi:10.1017/S0022112008001328.
- [42] M.T. Lim, R.W. Anderson, V.S. Arpaci, Prediction of Spark Kernel Development in Constant Volume Combustion, *Combust. Flame*. 69 (1987) 303–316.
- [43] J. Kim, *The Role of Radicals Supplied Directly and Indirectly on Ignition*, Georgia Institute of Technology, 2014.
- [44] F. Migliorini, S. Deiuliis, F. Cignoli, G. Zizak, How “flat” is the rich premixed flame produced by your McKenna burner?, *Combust. Flame*. 153 (2008) 384–393. doi:10.1016/j.combustflame.2008.01.007.
- [45] G. Hartung, J. Hult, C.F. Kaminski, A flat flame burner for the calibration of laser thermometry techniques, *Meas. Sci. Technol.* 17 (2006) 2485–2493. doi:10.1088/0957-0233/17/9/016.
- [46] P. Weigand, R. Lückcrath, W. Meier, *Documentation of Flat Premixed Laminar CH<sub>4</sub>/Air Standard Flames: Temperatures and Species Concentrations*, Stuttgart, 2003.
- [47] C. Brackmann, J. Bood, P.-E. Bengtsson, T. Seeger, M. Schenk, A. Leipertz, Simultaneous vibrational and pure rotational coherent anti-stokes Raman spectroscopy for temperature and multispecies concentration measurements demonstrated in sooting flames., *Appl. Opt.* 41 (2002) 564–72. <http://www.ncbi.nlm.nih.gov/pubmed/11905583>.
- [48] F. Migliorini, P. Giuliani, S. De Iuliis, F. Cignoli, G. Zizak, Hydrogen addition in a rich premixed ethylene-air flame, Milan, n.d. [http://www.aivela.org/Zizak\\_paper03.pdf](http://www.aivela.org/Zizak_paper03.pdf).
- [49] V. Hinasageri, R.P. Vedula, S. V Prabhu, Thermocouple error correction for measuring the flame temperature with determination of emissivity and heat transfer coefficient., *Rev. Sci. Instrum.* 84 (2013) 024902. doi:10.1063/1.4790471.

- [50] F. White, *Viscous Fluid Flow*, Third, McGraw Hill, 2006.
- [51] F. McClintock, S. Kline, Describing uncertainties in single-sample experiments, *Mech. Eng.* 75 (1953) 3–8.
- [52] C.K. Law, *Combustion Physics*, 1st ed., Cambridge University Press, 2006.
- [53] R. Sau, K. Mahesh, Passive scalar mixing in vortex rings, *J. Fluid Mech.* 582 (2007) 449. doi:10.1017/S0022112007006349.
- [54] I. Choutapalli, a. Krothapalli, J.H. Arakeri, An experimental study of an axisymmetric turbulent pulsed air jet, *J. Fluid Mech.* 631 (2009) 23. doi:10.1017/S0022112009007009.
- [55] P.F. Linden, J.S. Turner, The formation of “optimal” vortex rings, and the efficiency of propulsion devices, *J. Fluid Mech.* 427 (2001) 61–72. doi:10.1017/S0022112000002263.
- [56] Y.K. Chang, a. D. Vakili, Dynamics of vortex rings in crossflow, *Phys. Fluids.* 7 (1995) 1583. doi:10.1063/1.868545.
- [57] L. Gan, T.B. Nickels, J.R. Dawson, An experimental study of a turbulent vortex ring: a three-dimensional representation, *Exp. Fluids.* 51 (2011) 1493–1507. doi:10.1007/s00348-011-1156-5.
- [58] R. Sau, K. Mahesh, Optimization of pulsed jets in crossflow, *J. Fluid Mech.* 653 (2010) 365–390. doi:10.1017/S0022112010000388.
- [59] M. Ilak, P. Schlatter, S. Bagheri, D.S. Henningson, Bifurcation and stability analysis of a jet in cross-flow: onset of global instability at a low velocity ratio, *J. Fluid Mech.* 696 (2012) 94–121. doi:10.1017/jfm.2012.10.
- [60] R.F. Huang, J. Lan, Characteristic modes and evolution processes of shear-layer vortices in an elevated transverse jet, *Phys. Fluids.* 17 (2005). doi:10.1063/1.1852575.

- [61] Y.B. Zeldovich, The Physics of the Combustion of Gases, Zh. Eksp. Teor. Fiz. 159 (1941).

## Appendices

### Appendix A: Integration Time Calculations

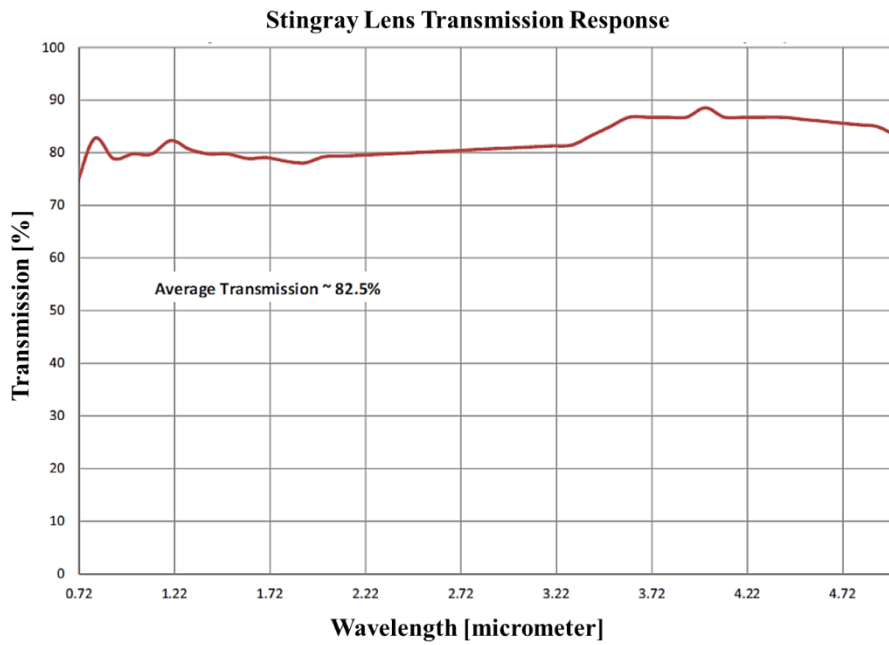
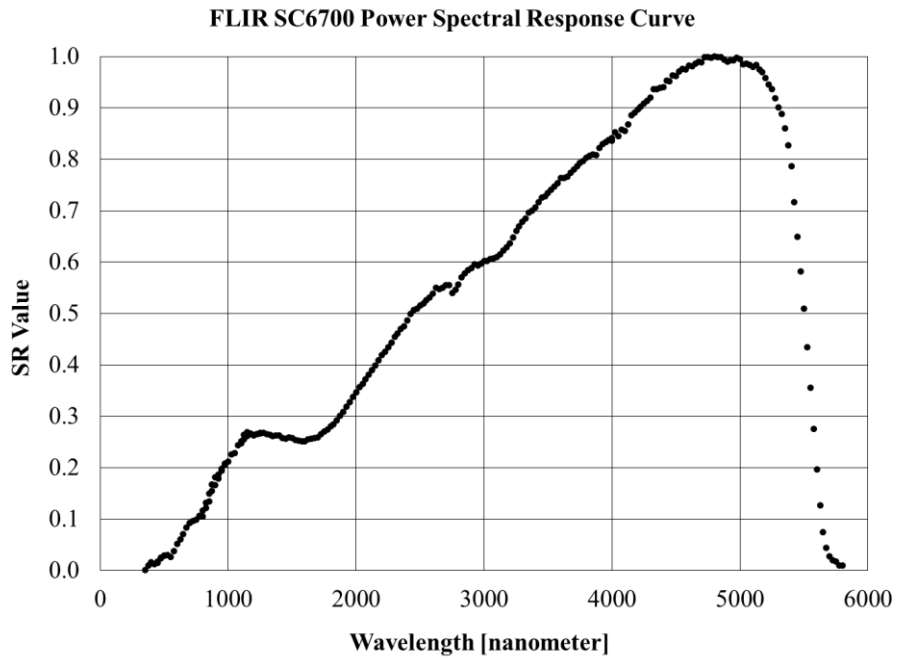
The integration time for the IR camera was determined under the pretext of lessening spatial blurring effects. Smoothed edges and incorrect averaging are a few consequences of detecting an object's motion. The following equation was used to calculate the integration time,

$$t_{\text{int}} = \frac{d}{V_{\text{C.F.}}}$$

Here,  $V_{\text{C.F.}}$  was selected at the maximum cross-flow velocity (e.g., 15.6 m/s) and  $d$  was designated the tolerance for allowable spatial shift. Less than a 10 percent spatial shift based the igniter diameter (i.e., 1.288 mm) was deemed appropriate considering experimental constraints and influence on radiation intensity measurements. Therefore, the maximum integration time that would remain within the tolerance specified is,

$$t_{\text{int}} = \frac{1.288\text{mm}}{15.6\text{m/s}} = 0.0825\text{ms} .$$

## Appendix B: Spectral Absorption of Optical Equipment



### **Appendix C: Psychrometric and Chemical Composition Analysis**

Water vapor concentration in room air was used to determine the temperature of spark kernels. Measurements of relative humidity ( $\phi$ ) and ambient temperature of air were collected. The saturated pressure ( $P_g$ ) was calculated using the ambient temperature. The vapor pressure ( $P_v$ ) was determined from the product of  $\phi$  and  $P_g$ . Lastly, the water vapor concentration was the quotient of  $P_v$  and atmospheric pressure.

The solution of RADCAL [32] is dependent on the chemical composition of five constituents: oxygen, nitrogen, carbon dioxide, water vapor, and methane. The concentration of carbon dioxide was measured in parts per million, which was easily converted to mole fraction by dividing the measurement by 1,000,000. Oxygen was defined from the Handbook of Chemistry and Physics value. This work assumes that methane concentrations in ambient air are negligible, thereby leaving the concentration of nitrogen as a variable. Convergence criteria of RADCAL is that the sum of all the concentrations (in mole fraction) is less than 1. Thus, nitrogen was defined from the remaining concentration.

## Appendix D: Interpolation Database Code

```

%%%% INTERPOLATION DATABASE %%%
% THIS CODE WILL OUTPUT DAY-SPECIFIC INTERPOLATION DATABASE (.MAT)
% CONTAINING PATH LENGTH, TEMPERATURE, AND INTENSITY

clc
clear
close all

Time_elapse = tic; % INITIALIZE COMPLETION TIME

% READ TRANSMISSION RESPONSE OF STINGRAY LENS
STR=dlmread('stingray transmission response FULL II.txt');
x_str=STR(:,1); % WAVELENGTH (MICROMETER)
y_str=STR(:,2); % TRANSMISSIVITY (%)

holdup=0;
tickera=1;
tickerb=0;

% REARRANGE DATA IN ACCENDING ORDER, DELETE REPEAT VALUES
for iota=1:length(x_str)-1

    if x_str(iota)==x_str(iota+1)
        tickerb=tickerb+1;
        yavg(tickerb)=y_str(iota);
        holdup=1;
    elseif x_str(iota)~=0 && holdup==1
        xn(tickera)=x_str(iota);
        yn(tickera)=mean(yavg);
        tickera=tickera+1;
        clear yavg
        holdup=0;
        yavg=0;
        tickerb=0;
    else
        xn(tickera)=x_str(iota);
        yn(tickera)=y_str(iota);
        tickera=tickera+1;
        holdup=0;
    end
end

end

% READ FLIR SC6700 DETECTOR REPONSE
STR1=dlmread('ASCII for detector responseIIII.txt');
x_str1=STR1(:,1);
y_str1=STR1(:,2);

holdup1=0;
tickera1=1;
tickerb1=0;

```

```

for iotal=1:length(x_str1)-1

    if x_str1(iotal)==x_str1(iotal+1)
        tickerb1=tickerb1+1;
        yavg1(tickerb1)=y_str1(iotal);
        holdup1=1;
    elseif x_str1(iotal)~=0 && holdup1==1
        xn1(tickeral)=x_str1(iotal);
        yn1(tickeral)=mean(yavg1);
        tickeral=tickeral+1;
        clear yavg1
        holdup1=0;
        yavg1=0;
        tickerb1=0;
    else
        xn1(tickeral)=x_str1(iotal);
        yn1(tickeral)=y_str1(iotal);
        tickeral=tickeral+1;
        holdup1=0;
    end
end

end

%%
fi=100; % THIS NUMBER SQUARED WILL BE THE NUMBER OF DATA POINTS IN THE
% DATABASE
path=linspace(0.001,0.04,fi); % VARY PATH LENGTHS BETWEEN 1 mm TO 4 cm
pL=length(path);

temp=linspace(400,4000,fi); % VARY TEMPERATURE BETWEEN 400-4000 KELVIN
tempL=length(temp);

inten=linspace(.1,50,fi); % VARY INTENSITY BETWEEN 0.1-50 W/m^2-sr
intenL=length(inten);

trends=zeros(3,tempL,pL);
tempa=zeros(pL,intenL);
emislens=zeros(227,1);

% DATABASE CONSTRUCTED IN THIS LOOP
for j=1:pL
    trendi=zeros(3,tempL);
    for k=1:tempL
        temperature=temp(k);
        pathlength=path(j);

        % RADCAL
        input=dlmread('input.txt'); % CONTAINS PATH LENGTH, 5 CHEMICAL
        % CONCENTRAIONS, AND TEMPERATURE
        w=dlmread('input_wavelengths.txt'); % WAVELENGTHS OF INTEREST
        input(1)=pathlength;
        input(7)=temperature;
    end
end

```

```

dlmwrite('input.txt',input)
system('radcal.exe'); % RUN RADCAL
clc
a=dlmread('forward.txt'); % SOLUTION OF RADCAL

for i=1:length(w)
    stinglens=interp1(xn,yn,w(i),'pchip');
    flir=interp1(xn1,yn1,w(i),'pchip');
    emislens(i)=stinglens*flir*a(i,2); % ACCOUNTING FOR DETECTOR
    % AND LENS LOSSES IN INTENSITY (W/m^2-sr-micrometer)
end

sums=trapz(w,emislens); % INTEGRATED INTENSITY
intensity=sums;

trendi(1,k)=intensity;
trendi(2,k)=pathlength;
trendi(3,k)=temperature;

end

trenda(:,:,j)=trendi;
temperaturei=interp1(trenda(1,:,j),trenda(3,:,j),inten,'pchip');
tempa(j,:)=temperaturei;

end

I=inten;
P=path;
[X,Y]=meshgrid(I,P);
Z=tempa;
% NAMING CONVENTION FOR DATABASE
save('interpolationv_9_15.mat','X','Y','Z')

```

## Appendix E: Deconvolution of Intensity to attain Temperature (DIT) Code

```

%% DECONVOLUTION OF INTENSITY TO ATTAIN TEMPERATURE (DIT)
% THIS CODE WILL OUTPUT TEMPERATURE OF SPARK KERNELS FROM RAW IR IMAGES

clear
clc
close all
%% INITIALIZE RAW IR IMAGES
movienum=528; % MANUALLY ENTER MOVIE NUMBER
Time_elapse = tic;
n=load('Raw_Data_528.mat'); % MANUALLY ENTER NAME OF DATA
data_raw=n.data_raw;

data_test=single(data_raw);
data_test(data_test<3900)=NaN; % THIS IS USED TO VISUALIZE EMBERS IN IR
% IMAGES

start=1;
finish=size(data_raw,3);

% NAMING CONVENTION FOR ALL OUPUT FILES
tempnamefull=sprintf('Temp_final_%i.mat',movienum);
centroidfull=sprintf('Centroid_final_%i.mat',movienum);
centroidpartial=sprintf('Centroid_final_partial_%i.mat',movienum);
intensityfull=sprintf('Inten_final_%i.mat',movienum);
appsizefull=sprintf('Apparent_size_final_%i.mat',movienum);
energyfull=sprintf('Sensible_energy_final_%i.mat',movienum);
%% FILTER THROUGH DATA TO DETERMINE SPARK EVENT

tic1=0;
for j=start:finish-1
    % SEARCHING FOR PLASMA GENERATION ABOVE/BELOW TOLERANCE
    m=max(max(data_raw(:,97:end,j+1)))-max(max(data_raw(:,97:end,j)));
    if m>3000 && m<=6000 % USER DEFINED PHOTON COUNT LIMITS, THIS IS
        % USED TO ENSURE THE KERNEL RIGHT AFTER PLASMA IS EVALUATED
        tic1=tic1+1;
        flag(tic1)=j;
    elseif m>6000
        tic1=tic1+1;
        flag(tic1)=j+1;
    end
end

tic2=0;
tic3=0;
for k=2:length(flag)
    tic2=tic2+1;
    diff(tic2)=flag(k)-flag(k-1);
    if diff(tic2)>1
        tic3=tic3+1;
        event(tic3)=flag(k-1);
    end
end

```

```

    if k==length(flag)
        tic3=tic3+1;
        event(tic3)=flag(k);
    end
end

%% VISUALLY SEARCH FOR EMBERS IN DATA
for ja=1:length(event)
    figure
    contourf(data_test(:,:,event(ja)+1),25,'edgecolor','none')
    axis equal
    colorbar
    colormap jet
    caxis([3000 6000])
    title(sprintf('Event: %i',ja))

    pause
    close all
end

% DELETE EVENTS WITH EMBERS IN DECENDING ORDER
event(30)=[];
event(13)=[];
event(12)=[];
event(11)=[];
event(7)=[];
event(6)=[];

%% CONVERT PHOTON COUNTS TO RADIATION INTENSITY OF ONLY KERNELS
PHOTON_BKG=zeros(size(data_raw,1),size(data_raw,2),length(event));
INTENSITY_BKG=zeros(size(data_raw,1),size(data_raw,2),length(event));
for i=1:length(event)
    range=(event(i)-2):(event(i)-1);    % RANGE FOR BACKGROUND AVERAGE WITH
    % SMALL INTEGRATION TIME
    PHOTON_BKG(:,:,i)=mean(single(data_raw(:,:,range)),3);
    % AVERAGE BACKGROUND INTENSITY THAT IS SPARK EVENT SPECIFIC, MANUALLY
    % ENTER BLACKBODY CALIBRATION CURVE FIT
    INTENSITY_BKG(:,:,i)=single(((6.7996e-3).*PHOTON_BKG(:,:,i))-(7.5655));
    for j=(event(i)+1):(event(i)+5)    % 5 FRAMES OF DETECTED KERNELS AFTER
        % PLASMA GENERATION
        % INTENSITY OF ENTIRE IR IMAGE
        INTENSITY_RAW(:,:,j)=(6.7996e-3).*single(data_raw(:,:,j))-(7.5655);
        % BACKGROUND SUBTRACTED INTENSITY, ONLY THE INTENSITY OF THE KERNEL
        % IS DETERMINED
        INTENSITY_SUBTRACTION(:,:,j)=single(INTENSITY_RAW(:,:,j))...
            -single(INTENSITY_BKG(:,:,i));
    end
end

tic4=0;
tic5=0;

for i=event
    tic5=tic5+1;
    for j=1:5    % THIS IS THE AVERAGE NUMBER OF STATISTICAL FRAMES PER

```

```

    % SPARK EVENT
    tic4=tic4+1;
    frameindex(tic4)=i+j;

tempname{frameindex(tic4)}=sprintf('Temp_%i_%i_%i.csv',movienum,tic5,j);
    end
end

nmn=single(INTENSITY_SUBTRACTION(:,:,frameindex));
save(intensityfull,'nmn') % SAVE BACKGROUND SUBTRACTED INTENSITIES FOR
% EACH SPARK EVENT

%% DIT
clear PHOTON_BKG INTENSITY_RAW INTENSITY_BKG data_raw nmn diff data_test
bifurcation=zeros(length(frameindex),1);
lastrowkern=60; % CUT-OFF
lastcolkern=17; % CUT-OFF
T_inf=28.1+273; % DAY-SPECIFIC ROOM TEMPERATURE

for frame=21:22 % 1:length(frameindex)
    thetamid=single(INTENSITY_SUBTRACTION(:,:,frameindex(frame)));
    [Yyy,Xxx]=size(thetamid);
    % INTENSITY FROM THE MIRROR
    thetapre=thetamid(:,1:(Xxx/2-lastcolkern))./(.85); % 0.85 IS BECAUSE
    % OF THE REFLECTION LOSSES OF THE MIRROR
    % INTENSITY FROM LINE-OF-SIGHT
    thetapost=thetamid(:,(Xxx/2-lastcolkern+1):Xxx);
    theta=[thetapre thetapost];
    flag=0;
    iter=0;
    kernlhs=.12;
    kernrhs=.1;

    [Y,X]=size(theta);
    leh=(size(theta,2))/2-5;
    Temperature = zeros(Y,leh);
    senergy=zeros(Y,leh);
    thetabin=zeros(Y,X);

    % BINARIZE KERNELS
    for i=1:X*Y
        if i<=6144 % THIS IS THE LOCATION OF THE MIRROR EDGE
            if theta(i)<kernlhs
                theta(i)=0;
                thetabin(i)=0;
            else
                thetabin(i)=1;
            end
        elseif i>6144
            if theta(i)<kernrhs
                theta(i)=0;
                thetabin(i)=0;
            else
                thetabin(i)=1;
            end
        end
    end
end

```

```

    end
end

thetalpre=thetabin(:,1:(X/2-lastcolkern)); % BINARIZED LEFT IMAGE
theta2pre=thetabin(:,(X/2+4):(X-2)); % BINARIZED RIGHT IMAGE
thetah=theta(:,(X/2+4):(X-2)); % RIGHT INTENSITY IMAGE

% ELIMATE ARTIFACTS IN REFLECTED IMAGES
cd=bwconncomp(thetalpre,4);
ld=labelmatrix(cd);
dd=cd.PixelIdxList;
[xdd,ydd]=size(dd);
for kappad=1:ydd
    if length(dd{1,kappad})<50
        dd{1,kappad}=5;
    end
end
cd.('PixelIdxList')=dd;
ldd=labelmatrix(cd);
ldd(ldd>0)=1;
thetal=ldd;

% ELIMATE ARTIFACTS IN LINE-OF-SIGHT IMAGES
ce=bwconncomp(theta2pre,4);
le=labelmatrix(ce);
% bi=cd.NumObjects;
de=ce.PixelIdxList;
[xde,yde]=size(de);
for kappae=1:yde
    if length(de{1,kappae})<25
        de{1,kappae}=5;
    end
end
ce.('PixelIdxList')=de;
lde=labelmatrix(ce);
lde(lde>0)=1;
theta2=lde;

% DETERMINE THE SIZE OF KERNELS
kern_size(frame)=sum(sum(theta2(1:lastrowkern,:)))/(1.74^2);

row1=sum(thetal,2);
row2=sum(theta2,2);

jeez=thetah;
jeez(jeez==0)=NaN;

thetahp=zeros(Y,leh);

pathlength=cell(length(row1),1);

% DETERMINE THE PATH LENGTH AT EACH DISCRETE LOCATION
for i=1:length(row1)
    D=row1(i);

```

```

Delta=row2(i);

if Delta==0 || D==0
    pathlength{i}=0;
else
    width=1:Delta;
    r=(Delta+1)/2;
    for j=1:Delta % DETERMINING WHICH LENGTH IS LONGER
        if Delta>D
            b=D/2;
            a=Delta/2;
        else
            a=D/2;
            b=Delta/2;
        end

        dx(j)=abs(j-r);
        s(j)=sqrt(b^2-b^2/a^2*dx(j)^2); % EQUATION OF OVAL
        s(j)=2*s(j);
        S(j)=s(j)/(1.74*1000); % CONVERTING PIXEL TO METERS
        if S(j)<0.0012 % MINIMUM LENGTH, BASED ON THE
            % SIZE OF PIXEL MULTIPLY BY 2 FOR CONFIDENCE
            S(j)=0.0012;
        end
    end

    pathlength{i}=S;
    clear s
    clear S
end
end

for m=1:Y
    pathcol=pathlength{m};
    if pathcol==0
    else
        step=0;
        for n=1:leh
            if theta2(m,n)==0
            else
                step=step+1;
                thetahp(m,n)=pathcol(step);
            end
        end
    end
end

thetahp=single(thetahp);
gory=thetahp;
gory(gory==0)=NaN; % FOR PLOTTING THE PATH LENGTH DISTRIBUTION

%% APPLYING INTERPOLATION DATABASE TO DETERMINE TEMPERATURE
Ypix=Y;
Xpix=X;
clear X Y

```

```

load('interpolationv_9_13')    % LOAD INTERPOLATION DATABASE

for z = 1:Ypix
    for q = 1:leh
        p=thetahp(z,q);
        i=single(thetah(z,q));
        if i>0 && p>0
            % TEMPERATURE OF KERNEL
            Temperature(z,q)=interp2(X,Y,Z,i,p,'cubic');
            % SENSIBLE ENERGY OF KERNEL
            senergy(z,q)=p*((1.74*1000)^-
2)*101300/286.9/Temperature(z,q)*...
            ((1.6645e-
4)*Temperature(z,q)+1.005)*1000*(Temperature(z,q)-T_inf);    % x1000 TO PUT
INTO JOULES

            end
        end
    end
    tempall(:, :, frame)=single(Temperature);
    SEnergy(:, :, frame)=single(senergy);

    save(tempnamefull, 'tempall')
    save(appsizefull, 'kern_size')
    save(energyfull, 'SEnergy')

    % DETERMINE THE CENTROID OF DETECTED KERNELS
    theta_cent=thetah(1:60,:);
    theta_cent(theta_cent<kernrhs)=0;
    W(frame)=sum(sum(theta_cent));

    for zz=1:size(theta_cent,1)
        for qq=1:size(theta_cent,2)
            centxi(zz,qq)=theta_cent(zz,qq)*(qq-.5)/W(frame);
            centyi(zz,qq)=theta_cent(zz,qq)*(zz-.5)/W(frame);
            % -.5 BECAUSE THAT IS WHERE THE CENTER OF MASS IS OCCURRING AT
            % THAT SPECIFIC LOCATION
        end
    end
    X_bar(frame)=sum(sum(centxi));
    Y_bar(frame)=sum(sum(centyi));

    if isnan(X_bar(frame))
        X_bar(frame)=[];
        Y_bar(frame)=[];
    end

    clear row1 row2 pathlength bi bifur yde
end

Full_time_DIT = toc(Time_elapse);
full_time_dit = num2str(Full_time_DIT);
hhh = msgbox({'Time to complete',full_time_dit,'seconds'});

```

```
X_centroid=X_bar;
X_centroid(X_centroid==0)=[];
Y_centroid=Y_bar;
Y_centroid(Y_centroid==0)=[];

[X_sorty, Sortindex]=sort(X_centroid);
Y_sorty=Y_centroid(Sortindex);

cent_roid=[X_sorty; Y_sorty];
cent_roid_pre=[X_bar; Y_bar];
save(centroidpartial, 'cent_roid_pre')
save(centroidfull, 'cent_roid')
```

## Appendix F: Additional Post Processing Codes

```

%%%%% AVERAGE KERNEL TEMPERATURE %%%%%
% THIS CODE WILL OUTPUT SINGLE AVERAGE KERNEL TEMPERATURE DISTRIBUTION
% USING THE STATISTICAL PARAMETER "n"

clear
clc

% LOAD TEMPERATURE .MAT FILES DETERMINED FROM DIT CODE
n_1=load('Temp_final_518.mat');
n_2=load('Temp_final_519.mat');
n_3=load('Temp_final_520.mat');
n_4=load('Temp_final_527.mat');
n_13=load('Temp_final_521.mat');
n_14=load('Temp_final_526.mat');
n_15=load('Temp_final_528.mat');
n_16=load('Temp_final_529.mat');

n_9=load('Temp_final_535.mat');
n_10=load('Temp_final_536.mat');
n_11=load('Temp_final_537.mat');
n_17=load('Temp_final_538.mat');

n_18=load('Temp_finaltest15_319.mat');
n_19=load('Temp_finaltest15_320.mat');
n_20=load('Temp_finaltest15_328.mat');
n_21=load('Temp_finaltest15_329.mat');

% ASSIGN TEMPERATURE ARRAYS FROM .MAT FILE
T_1=n_1.tempall;
z1=size(T_1,3);
T_2=n_2.tempall;
z2=size(T_2,3);
T_3=n_3.tempall;
z3=size(T_3,3);
T_4=n_4.tempall;
z4=size(T_4,3);
T_13=n_13.tempall;
z13=size(T_13,3);
T_14=n_14.tempall;
z14=size(T_14,3);
T_15=n_15.tempall;
z15=size(T_15,3);
T_16=n_16.tempall;
z16=size(T_16,3);

T_9=n_9.tempall;
T_9=circshift(T_9, [-2 -2]); % THIS LINE ENSURES THAT THE ORIGIN OF THE
% IGNITER IS UNIFORM ACROSS ALL DATA SETS
z9=size(T_9,3);
T_10=n_10.tempall;
T_10=circshift(T_10, [-2 -2]);
z10=size(T_10,3);

```

```

T_11=n_11.tempall;
T_11=circshift(T_11, [-2 -2]);
z11=size(T_11,3);
T_17=n_17.tempall;
T_17=circshift(T_17, [-2 -2]);
z17=size(T_17,3);

T_18=n_18.tempall;
z18=size(T_18,3);
T_19=n_19.tempall;
z19=size(T_19,3);
T_20=n_20.tempall;
z20=size(T_20,3);
T_21=n_21.tempall;
z21=size(T_21,3);

% CONCATENATE TEMPERATURE IN 3RD DIMENSION
T=single(cat(3,T_1,T_2,T_3,T_4,T_13,T_14,T_15,T_16,T_9,T_10,T_11,T_17,T_18,T_
19,T_20,T_21));

[sy,sx,sz]=size(T);

% INITIALIZE BINARY MATRIX
Tbin=single(zeros(sy,sx,sz));

for frame=1:sz

    for i=1:sy
        for j=1:sx
            if T(i,j,frame)>300 % IF VALUE IS GREATER THAN 300 KELVIN
                Tbin(i,j,frame)=1; % ASSIGN IT A 1
            elseif isnan(T(i,j,frame))
                Tbin(i,j,frame)=NaN;
            else % IF VALUE IS LESS THAN 300 KELVIN
                Tbin(i,j,frame)=NaN; % ASSIGN IT A NaN
            %
                T(i,j,frame)=NaN;
            end
        end
    end
end

sumtempbin=nansum(Tbin,3); % SUM IN 3RD DIMENSION, OUTPUTS 2-D MATRIX
% THAT REPRESENTS THE NUMBER OF TIMES A TEMPERATURE VALUE GREATER THAN
% 300 KELVIN WAS DETECTED AT A SPECIFIC LOCATION

% INITIALIZE AVERAGE TEMPERATURE MATRIX
Avg_temperature=zeros(sy,sx);
% ANY VALUES EQUAL TO OR LESS THEN 0 KELVIN ARE NaN (MAY OCCUR IN DIT
% CODE)
T(T<0)=NaN;
T(T==0)=NaN;

```

```

for i=1:sy
    for j=1:sx
        if sumtempbin(i,j)>98 % 98 IS THE STATISTICAL PARAMETER "n", REFER
TO THESIS FOR EQUATION
            % AVERAGE THE TEMPERATRE AT (ROW, COL) IF GREATER THAN
            % 98 DETECTED TEMPERATURES AT SAME (ROW, COL)
            Avg_temperature(i,j)=nanmean(T(i,j,:),3);
        else % OTHERWISE, ASSIGN NaN
            Avg_temperature(i,j)=NaN;
        end
    end
end
% IN CASE TEMPERATURES BELOW 300 KELVIN SLIPPED THROUGH
Avg_temperature(Avg_temperature<300)=NaN;

[Y_s,X_s]=size(Avg_temperature);
X_loc=1:X_s;
Y_loc=1:Y_s;
% RE-ASSIGN LOCATION OF AVERAGE TEMPERATURE FROM PIXEL TO IGNITER DIAMETERS
% IGNITER CENTER AT (35,7)
X_center=(X_loc-35)/1.74)/12.88; % 12.88 IS THE DIAMETER OF IGNITER
Y_center=(Y_loc-7)/1.74)/12.88; % 1.74 IS RESOLUTION (PIX/MM)

figure
contourf(X_center,Y_center,rot90(Avg_temperature,2),50,'edgecolor','none')
% ROT90 USED BECAUSE IGNITER WAS POINTED DOWNWARD NORMAL, IT FLIPS PLOT TO
% SHOW KERNELS EJECTED IN UPWARD NORMAL DIRECTION
v=colorbar;
ylabel(v,'Temperature [K]')
caxis([600 1000]);
axis equal
xlim([-1.5 1.5])
ylim([0 3])
colormap jet
xlabel('x/D')
ylabel('y/D')
set(gca,'fontsize',24)

% EXTRA PLOTTING FEATURES USED IN THESIS (UNCOMMENT AS NECESSARY)
% v.Ticks=[];
% ylabel(v,'Increasing Temperature \rightarrow')
% clim = get(v,'Ylim');
% set(gca,'YTickLabel',[])
% title({'Downward Normal';'Igniter Orientation [-y]'})
% title('Combined Average')

%%% PHASE AVERAGE KERNEL TEMPERATURES %%%
% THIS CODE WILL OUTPUT PHASE AVERAGE KERNEL TEMPERATURE DISTRIBUTIONS
% USING THE STATISTICAL PARAMETER "n"

clear
clc

```

```

% LOAD TEMPERATURE .MAT FILES DETERMINED FROM DIT CODE
n_1=load('Temp_final_518.mat');
n_2=load('Temp_final_519.mat');
n_3=load('Temp_final_520.mat');
n_4=load('Temp_final_527.mat');
n_13=load('Temp_final_521.mat');
n_14=load('Temp_final_526.mat');
n_15=load('Temp_final_528.mat');
n_16=load('Temp_final_529.mat');

n_9=load('Temp_final_535.mat');
n_10=load('Temp_final_536.mat');
n_11=load('Temp_final_537.mat');
n_17=load('Temp_final_538.mat');

n_18=load('Temp_finaltest15_319.mat');
n_19=load('Temp_finaltest15_320.mat');
n_20=load('Temp_finaltest15_328.mat');
n_21=load('Temp_finaltest15_329.mat');

% ASSIGN TEMPERATURE ARRAYS FROM .MAT FILE
T_1=n_1.tempall;
z1=size(T_1,3);
T_2=n_2.tempall;
z2=size(T_2,3);
T_3=n_3.tempall;
z3=size(T_3,3);
T_4=n_4.tempall;
z4=size(T_4,3);
T_13=n_13.tempall;
z13=size(T_13,3);
T_14=n_14.tempall;
z14=size(T_14,3);
T_15=n_15.tempall;
z15=size(T_15,3);
T_16=n_16.tempall;
z16=size(T_16,3);

T_9=n_9.tempall;
T_9=circshift(T_9, [-2 -2]); % THIS LINE ENSURES THAT THE ORIGIN OF THE
% IGNITER IS UNIFORM ACROSS ALL DATA SETS
z9=size(T_9,3);
T_10=n_10.tempall;
T_10=circshift(T_10, [-2 -2]);
z10=size(T_10,3);
T_11=n_11.tempall;
T_11=circshift(T_11, [-2 -2]);
z11=size(T_11,3);
T_17=n_17.tempall;
T_17=circshift(T_17, [-2 -2]);
z17=size(T_17,3);

T_18=n_18.tempall;
z18=size(T_18,3);
T_19=n_19.tempall;

```

```

z19=size(T_19,3);
T_20=n_20.tempall;
z20=size(T_20,3);
T_21=n_21.tempall;
z21=size(T_21,3);

% ARRAY OF NUMBER OF SPARK EVENTS, 1 EVENT CONTAINS 5 PROFILES
matrixsizes=[z1/5-1 z2/5-1 z3/5-1 z4/5-1 z13/5-1 z14/5-1 z15/5-1 z16/5-1
z9/5-1 z10/5-1 z11/5-1 z17/5-1 z18/5-1 z19/5-1 z20/5-1 z21/5-1]; % z6/5-1
z7/5-1 z8/5-1 z9/5-1 z10/5-1 z11/5-1 z12/5-1];

% INITIALIZE TEMPERATURE MATRICES BASED ON PHASE OF SPARK EVENT (I.E. 1ST
% TEMPERATURE PROFILE AFTER DETECTING PLASMA, LAST PROFILE EVALUATED)
Int_11=zeros(size(T_1,1),size(T_1,2),matrixsizes(1));
Int_21=zeros(size(T_1,1),size(T_1,2),matrixsizes(1));
Int_31=zeros(size(T_1,1),size(T_1,2),matrixsizes(1));
Int_41=zeros(size(T_1,1),size(T_1,2),matrixsizes(1));
Int_51=zeros(size(T_1,1),size(T_1,2),matrixsizes(1));

Int_12=zeros(size(T_2,1),size(T_1,2),matrixsizes(2));
Int_22=zeros(size(T_2,1),size(T_1,2),matrixsizes(2));
Int_32=zeros(size(T_2,1),size(T_1,2),matrixsizes(2));
Int_42=zeros(size(T_2,1),size(T_1,2),matrixsizes(2));
Int_52=zeros(size(T_2,1),size(T_1,2),matrixsizes(2));

Int_13=zeros(size(T_3,1),size(T_1,2),matrixsizes(3));
Int_23=zeros(size(T_3,1),size(T_1,2),matrixsizes(3));
Int_33=zeros(size(T_3,1),size(T_1,2),matrixsizes(3));
Int_43=zeros(size(T_3,1),size(T_1,2),matrixsizes(3));
Int_53=zeros(size(T_3,1),size(T_1,2),matrixsizes(3));

Int_14=zeros(size(T_3,1),size(T_1,2),matrixsizes(4));
Int_24=zeros(size(T_3,1),size(T_1,2),matrixsizes(4));
Int_34=zeros(size(T_3,1),size(T_1,2),matrixsizes(4));
Int_44=zeros(size(T_3,1),size(T_1,2),matrixsizes(4));
Int_54=zeros(size(T_3,1),size(T_1,2),matrixsizes(4));

Int_113=zeros(size(T_3,1),size(T_1,2),matrixsizes(5));
Int_213=zeros(size(T_3,1),size(T_1,2),matrixsizes(5));
Int_313=zeros(size(T_3,1),size(T_1,2),matrixsizes(5));
Int_413=zeros(size(T_3,1),size(T_1,2),matrixsizes(5));
Int_513=zeros(size(T_3,1),size(T_1,2),matrixsizes(5));

Int_114=zeros(size(T_3,1),size(T_1,2),matrixsizes(6));
Int_214=zeros(size(T_3,1),size(T_1,2),matrixsizes(6));
Int_314=zeros(size(T_3,1),size(T_1,2),matrixsizes(6));
Int_414=zeros(size(T_3,1),size(T_1,2),matrixsizes(6));
Int_514=zeros(size(T_3,1),size(T_1,2),matrixsizes(6));

Int_115=zeros(size(T_3,1),size(T_1,2),matrixsizes(7));
Int_215=zeros(size(T_3,1),size(T_1,2),matrixsizes(7));
Int_315=zeros(size(T_3,1),size(T_1,2),matrixsizes(7));
Int_415=zeros(size(T_3,1),size(T_1,2),matrixsizes(7));
Int_515=zeros(size(T_3,1),size(T_1,2),matrixsizes(7));

```



```
% MANUALLY ASSIGN FIRST SPARK EVENT IN PHASE DEPENDENT MATRICES
```

```
Int_11(:, :, 1)=T_1(:, :, 1);
Int_21(:, :, 1)=T_1(:, :, 2);
Int_31(:, :, 1)=T_1(:, :, 3);
Int_41(:, :, 1)=T_1(:, :, 4);
Int_51(:, :, 1)=T_1(:, :, 5);
```

```
Int_12(:, :, 1)=T_2(:, :, 1);
Int_22(:, :, 1)=T_2(:, :, 2);
Int_32(:, :, 1)=T_2(:, :, 3);
Int_42(:, :, 1)=T_2(:, :, 4);
Int_52(:, :, 1)=T_2(:, :, 5);
```

```
Int_13(:, :, 1)=T_3(:, :, 1);
Int_23(:, :, 1)=T_3(:, :, 2);
Int_33(:, :, 1)=T_3(:, :, 3);
Int_43(:, :, 1)=T_3(:, :, 4);
Int_53(:, :, 1)=T_3(:, :, 5);
```

```
Int_14(:, :, 1)=T_4(:, :, 1);
Int_24(:, :, 1)=T_4(:, :, 2);
Int_34(:, :, 1)=T_4(:, :, 3);
Int_44(:, :, 1)=T_4(:, :, 4);
Int_54(:, :, 1)=T_4(:, :, 5);
```

```
Int_113(:, :, 1)=T_13(:, :, 1);
Int_213(:, :, 1)=T_13(:, :, 2);
Int_313(:, :, 1)=T_13(:, :, 3);
Int_413(:, :, 1)=T_13(:, :, 4);
Int_513(:, :, 1)=T_13(:, :, 5);
```

```
Int_114(:, :, 1)=T_14(:, :, 1);
Int_214(:, :, 1)=T_14(:, :, 2);
Int_314(:, :, 1)=T_14(:, :, 3);
Int_414(:, :, 1)=T_14(:, :, 4);
Int_514(:, :, 1)=T_14(:, :, 5);
```

```
Int_115(:, :, 1)=T_15(:, :, 1);
Int_215(:, :, 1)=T_15(:, :, 2);
Int_315(:, :, 1)=T_15(:, :, 3);
Int_415(:, :, 1)=T_15(:, :, 4);
Int_515(:, :, 1)=T_15(:, :, 5);
```

```
Int_116(:, :, 1)=T_16(:, :, 1);
Int_216(:, :, 1)=T_16(:, :, 2);
Int_316(:, :, 1)=T_16(:, :, 3);
Int_416(:, :, 1)=T_16(:, :, 4);
Int_516(:, :, 1)=T_16(:, :, 5);
```

```
Int_19(:, :, 1)=T_9(:, :, 1);
Int_29(:, :, 1)=T_9(:, :, 2);
Int_39(:, :, 1)=T_9(:, :, 3);
Int_49(:, :, 1)=T_9(:, :, 4);
```

```

Int_59(:, :, 1)=T_9(:, :, 5);

Int_110(:, :, 1)=T_10(:, :, 1);
Int_210(:, :, 1)=T_10(:, :, 2);
Int_310(:, :, 1)=T_10(:, :, 3);
Int_410(:, :, 1)=T_10(:, :, 4);
Int_510(:, :, 1)=T_10(:, :, 5);

Int_111(:, :, 1)=T_11(:, :, 1);
Int_211(:, :, 1)=T_11(:, :, 2);
Int_311(:, :, 1)=T_11(:, :, 3);
Int_411(:, :, 1)=T_11(:, :, 4);
Int_511(:, :, 1)=T_11(:, :, 5);

Int_117(:, :, 1)=T_17(:, :, 1);
Int_217(:, :, 1)=T_17(:, :, 2);
Int_317(:, :, 1)=T_17(:, :, 3);
Int_417(:, :, 1)=T_17(:, :, 4);
Int_517(:, :, 1)=T_17(:, :, 5);

Int_118(:, :, 1)=T_18(:, :, 1);
Int_218(:, :, 1)=T_18(:, :, 2);
Int_318(:, :, 1)=T_18(:, :, 3);
Int_418(:, :, 1)=T_18(:, :, 4);
Int_518(:, :, 1)=T_18(:, :, 5);

Int_119(:, :, 1)=T_19(:, :, 1);
Int_219(:, :, 1)=T_19(:, :, 2);
Int_319(:, :, 1)=T_19(:, :, 3);
Int_419(:, :, 1)=T_19(:, :, 4);
Int_519(:, :, 1)=T_19(:, :, 5);

Int_120(:, :, 1)=T_20(:, :, 1);
Int_220(:, :, 1)=T_20(:, :, 2);
Int_320(:, :, 1)=T_20(:, :, 3);
Int_420(:, :, 1)=T_20(:, :, 4);
Int_520(:, :, 1)=T_20(:, :, 5);

Int_121(:, :, 1)=T_21(:, :, 1);
Int_221(:, :, 1)=T_21(:, :, 2);
Int_321(:, :, 1)=T_21(:, :, 3);
Int_421(:, :, 1)=T_21(:, :, 4);
Int_521(:, :, 1)=T_21(:, :, 5);

clear n_1 n_2 n_3 n_4 n_13 n_14 n_15 n_16 n_9 n_10 n_11 n_17 n_18 n_19 n_20
n_21

% ASSIGN ALL OTHER SPARK EVENTS (BASED ON OBSERVATIONS THAT SPARK EVENT
% CONTAINS 5 IMAGES AFTER DETECTING PLASMA)
for j=1:length(matrixsizes)
    for i=1:matrixsizes(j)
        if j==1
            Int_11(:, :, i+1)=single(T_1(:, :, 5*i+1));
            Int_21(:, :, i+1)=single(T_1(:, :, 5*i+2));

```

```

    Int_31(:, :, i+1)=single(T_1(:, :, 5*i+3));
    Int_41(:, :, i+1)=single(T_1(:, :, 5*i+4));
    Int_51(:, :, i+1)=single(T_1(:, :, 5*i+5));
elseif j==2
    Int_12(:, :, i+1)=single(T_2(:, :, 5*i+1));
    Int_22(:, :, i+1)=single(T_2(:, :, 5*i+2));
    Int_32(:, :, i+1)=single(T_2(:, :, 5*i+3));
    Int_42(:, :, i+1)=single(T_2(:, :, 5*i+4));
    Int_52(:, :, i+1)=single(T_2(:, :, 5*i+5));
elseif j==3
    Int_13(:, :, i+1)=single(T_3(:, :, 5*i+1));
    Int_23(:, :, i+1)=single(T_3(:, :, 5*i+2));
    Int_33(:, :, i+1)=single(T_3(:, :, 5*i+3));
    Int_43(:, :, i+1)=single(T_3(:, :, 5*i+4));
    Int_53(:, :, i+1)=single(T_3(:, :, 5*i+5));
elseif j==4
    Int_14(:, :, i+1)=single(T_4(:, :, 5*i+1));
    Int_24(:, :, i+1)=single(T_4(:, :, 5*i+2));
    Int_34(:, :, i+1)=single(T_4(:, :, 5*i+3));
    Int_44(:, :, i+1)=single(T_4(:, :, 5*i+4));
    Int_54(:, :, i+1)=single(T_4(:, :, 5*i+5));
elseif j==5
    Int_113(:, :, i+1)=single(T_13(:, :, 5*i+1));
    Int_213(:, :, i+1)=single(T_13(:, :, 5*i+2));
    Int_313(:, :, i+1)=single(T_13(:, :, 5*i+3));
    Int_413(:, :, i+1)=single(T_13(:, :, 5*i+4));
    Int_513(:, :, i+1)=single(T_13(:, :, 5*i+5));
elseif j==6
    Int_114(:, :, i+1)=single(T_14(:, :, 5*i+1));
    Int_214(:, :, i+1)=single(T_14(:, :, 5*i+2));
    Int_314(:, :, i+1)=single(T_14(:, :, 5*i+3));
    Int_414(:, :, i+1)=single(T_14(:, :, 5*i+4));
    Int_514(:, :, i+1)=single(T_14(:, :, 5*i+5));
elseif j==7
    Int_115(:, :, i+1)=single(T_15(:, :, 5*i+1));
    Int_215(:, :, i+1)=single(T_15(:, :, 5*i+2));
    Int_315(:, :, i+1)=single(T_15(:, :, 5*i+3));
    Int_415(:, :, i+1)=single(T_15(:, :, 5*i+4));
    Int_515(:, :, i+1)=single(T_15(:, :, 5*i+5));
elseif j==8
    Int_116(:, :, i+1)=single(T_16(:, :, 5*i+1));
    Int_216(:, :, i+1)=single(T_16(:, :, 5*i+2));
    Int_316(:, :, i+1)=single(T_16(:, :, 5*i+3));
    Int_416(:, :, i+1)=single(T_16(:, :, 5*i+4));
    Int_516(:, :, i+1)=single(T_16(:, :, 5*i+5));
elseif j==9
    Int_19(:, :, i+1)=single(T_9(:, :, 5*i+1));
    Int_29(:, :, i+1)=single(T_9(:, :, 5*i+2));
    Int_39(:, :, i+1)=single(T_9(:, :, 5*i+3));
    Int_49(:, :, i+1)=single(T_9(:, :, 5*i+4));
    Int_59(:, :, i+1)=single(T_9(:, :, 5*i+5));
elseif j==10
    Int_110(:, :, i+1)=single(T_10(:, :, 5*i+1));
    Int_210(:, :, i+1)=single(T_10(:, :, 5*i+2));
    Int_310(:, :, i+1)=single(T_10(:, :, 5*i+3));
    Int_410(:, :, i+1)=single(T_10(:, :, 5*i+4));

```

```

        Int_510(:,:,i+1)=single(T_10(:,:,5*i+5));
elseif j==11
    Int_111(:,:,i+1)=single(T_11(:,:,5*i+1));
    Int_211(:,:,i+1)=single(T_11(:,:,5*i+2));
    Int_311(:,:,i+1)=single(T_11(:,:,5*i+3));
    Int_411(:,:,i+1)=single(T_11(:,:,5*i+4));
    Int_511(:,:,i+1)=single(T_11(:,:,5*i+5));
elseif j==12
    Int_117(:,:,i+1)=single(T_17(:,:,5*i+1));
    Int_217(:,:,i+1)=single(T_17(:,:,5*i+2));
    Int_317(:,:,i+1)=single(T_17(:,:,5*i+3));
    Int_417(:,:,i+1)=single(T_17(:,:,5*i+4));
    Int_517(:,:,i+1)=single(T_17(:,:,5*i+5));
elseif j==13
    Int_118(:,:,i+1)=single(T_18(:,:,5*i+1));
    Int_218(:,:,i+1)=single(T_18(:,:,5*i+2));
    Int_318(:,:,i+1)=single(T_18(:,:,5*i+3));
    Int_418(:,:,i+1)=single(T_18(:,:,5*i+4));
    Int_518(:,:,i+1)=single(T_18(:,:,5*i+5));
elseif j==14
    Int_119(:,:,i+1)=single(T_19(:,:,5*i+1));
    Int_219(:,:,i+1)=single(T_19(:,:,5*i+2));
    Int_319(:,:,i+1)=single(T_19(:,:,5*i+3));
    Int_419(:,:,i+1)=single(T_19(:,:,5*i+4));
    Int_519(:,:,i+1)=single(T_19(:,:,5*i+5));
elseif j==15
    Int_120(:,:,i+1)=single(T_20(:,:,5*i+1));
    Int_220(:,:,i+1)=single(T_20(:,:,5*i+2));
    Int_320(:,:,i+1)=single(T_20(:,:,5*i+3));
    Int_420(:,:,i+1)=single(T_20(:,:,5*i+4));
    Int_520(:,:,i+1)=single(T_20(:,:,5*i+5));
else
    Int_121(:,:,i+1)=single(T_21(:,:,5*i+1));
    Int_221(:,:,i+1)=single(T_21(:,:,5*i+2));
    Int_321(:,:,i+1)=single(T_21(:,:,5*i+3));
    Int_421(:,:,i+1)=single(T_21(:,:,5*i+4));
    Int_521(:,:,i+1)=single(T_21(:,:,5*i+5));
end
end
end

% CLEAR NONCRITICAL MATRICES, THIS HELPS SPEED UP PROCESS
clear T_1 T_2 T_3 T_4 T_13 T_14 T_15 T_16 T_9 T_10 T_11 T_17 T_18 T_19 T_20
T_21

% CONCATENATE PROFILES BASED ON PHASE IN SPARK EVENT
INTENSITY_1=single(cat(3,Int_11,Int_12,Int_13,Int_14,Int_113,Int_114,Int_115,
Int_116,Int_19,Int_110,Int_111,Int_117,Int_118,Int_119,Int_120,Int_121));
INTENSITY_2=single(cat(3,Int_21,Int_22,Int_23,Int_24,Int_213,Int_214,Int_215,
Int_216,Int_29,Int_210,Int_211,Int_217,Int_218,Int_219,Int_220,Int_221));
%,Int_25)); %,Int_26,Int_27,Int_28,Int_29,Int_210,Int_211,Int_212));
INTENSITY_3=single(cat(3,Int_31,Int_32,Int_33,Int_34,Int_313,Int_314,Int_315,
Int_316,Int_39,Int_310,Int_311,Int_317,Int_318,Int_319,Int_320,Int_321));
%,Int_35)); %,Int_36,Int_37,Int_38,Int_39,Int_310,Int_311,Int_312));

```

```

INTENSITY_4=single(cat(3,Int_41,Int_42,Int_43,Int_44,Int_413,Int_414,Int_415,
Int_416,Int_49,Int_410,Int_411,Int_417,Int_418,Int_419,Int_420,Int_421));
%,Int_45)); %,Int_46,Int_47,Int_48,Int_49,Int_410,Int_411,Int_412));
INTENSITY_5=single(cat(3,Int_51,Int_52,Int_53,Int_54,Int_513,Int_514,Int_515,
Int_516,Int_59,Int_510,Int_511,Int_517,Int_518,Int_519,Int_520,Int_521));
%,Int_55));

```

```

INTENSITY_1(INTENSITY_1==0)=NaN;
INTENSITY_2(INTENSITY_2==0)=NaN;
INTENSITY_3(INTENSITY_3==0)=NaN;
INTENSITY_4(INTENSITY_4==0)=NaN;
INTENSITY_5(INTENSITY_5==0)=NaN;

```

```

% INITIALIZE BINARY MATRICES

```

```

[sy,sx,sz]=size(INTENSITY_1);
INTENSITY_1bin=single(zeros(sy,sx,sz));
INTENSITY_2bin=single(zeros(sy,sx,sz));
INTENSITY_3bin=single(zeros(sy,sx,sz));
INTENSITY_4bin=single(zeros(sy,sx,sz));
INTENSITY_5bin=single(zeros(sy,sx,sz));

```

```

% AVERAGE EACH PHASE IN THE 3RD DIMENSION (I.E. MULTIPLE SPARK EVENTS)
% PROCESS CAN SPEED UP IF "PARFOR" IS USED INSTEAD OF "FOR" FOR FRAME=1:SZ

```

```

for frame=1:sz
    for i=1:sy
        for j=1:sx
            if INTENSITY_1(i,j,frame)>300
                INTENSITY_1bin(i,j,frame)=1;
            else %if INTENSITY_1(i,j,frame)<.1
                INTENSITY_1bin(i,j,frame)=0;
            end
        end
    end
end

```

```

for frame=1:sz
    for i=1:sy
        for j=1:sx
            if INTENSITY_2(i,j,frame)>300
                INTENSITY_2bin(i,j,frame)=1;
            else %if INTENSITY_2(i,j,frame)<.1
                INTENSITY_2bin(i,j,frame)=0;
            end
        end
    end
end

```

```

for frame=1:sz
    for i=1:sy
        for j=1:sx
            if INTENSITY_3(i,j,frame)>300
                INTENSITY_3bin(i,j,frame)=1;
            else %if INTENSITY_3(i,j,frame)<0.1
                INTENSITY_3bin(i,j,frame)=0;
            end
        end
    end
end

```

```

        end
    end
end

for frame=1:sz
    for i=1:sy
        for j=1:sx
            if INTENSITY_4(i,j,frame)>300
                INTENSITY_4bin(i,j,frame)=1;
            else %if INTENSITY_4(i,j,frame)<.1
                INTENSITY_4bin(i,j,frame)=0;
            end
        end
    end
end

for frame=1:sz
    for i=1:sy
        for j=1:sx
            if INTENSITY_5(i,j,frame)>300
                INTENSITY_5bin(i,j,frame)=1;
            else %if INTENSITY_5(i,j,frame)<.1
                INTENSITY_5bin(i,j,frame)=0;
            end
        end
    end
end

INTENSITY_1bin(INTENSITY_1bin==0)=NaN;
INTENSITY_2bin(INTENSITY_2bin==0)=NaN;
INTENSITY_3bin(INTENSITY_3bin==0)=NaN;
INTENSITY_4bin(INTENSITY_4bin==0)=NaN;
INTENSITY_5bin(INTENSITY_5bin==0)=NaN;

% SUM IN 3RD DIMENSION, OUTPUTS 2-D MATRIX THAT REPRESENTS THE NUMBER OF
% TIMES A TEMPERATURE VALUE GREATER THAN 300 KELVIN WAS DETECTED AT A
% SPECIFIC LOCATION
sumtempbin_1=nansum(INTENSITY_1bin,3);
sumtempbin_2=nansum(INTENSITY_2bin,3);
sumtempbin_3=nansum(INTENSITY_3bin,3);
sumtempbin_4=nansum(INTENSITY_4bin,3);
sumtempbin_5=nansum(INTENSITY_5bin,3);

Avg_intensity_1=zeros(sy,sx);
Avg_intensity_2=zeros(sy,sx);
Avg_intensity_3=zeros(sy,sx);
Avg_intensity_4=zeros(sy,sx);
Avg_intensity_5=zeros(sy,sx);

clear Int_11 Int_12 Int_13 Int_14 Int_15

```

```

clear Int_21 Int_22 Int_23 Int_24 Int_25
clear Int_31 Int_32 Int_33 Int_34 Int_35
clear Int_41 Int_42 Int_43 Int_44 Int_45
clear Int_51 Int_52 Int_53 Int_54 Int_55

for i=1:sy
    for j=1:sx
        if sumtempbin_1(i,j)>98 % 98 IS THE STATISTICAL PARAMETER "n", REFER
TO THESIS FOR EQUATION
            % AVERAGE THE TEMPERATRE AT (ROW, COL) IF GREATER THAN
            % 98 DETECTED TEMPERATURES AT SAME (ROW, COL)
            Avg_intensity_1(i,j)=nanmean(INTENSITY_1(i,j,:),3);
        else
            Avg_intensity_1(i,j)=NaN;
        end
    end
end
for i=1:sy
    for j=1:sx
        if sumtempbin_2(i,j)>98
            Avg_intensity_2(i,j)=nanmean(INTENSITY_2(i,j,:),3);
        else
            Avg_intensity_2(i,j)=NaN;
        end
    end
end
for i=1:sy
    for j=1:sx
        if sumtempbin_3(i,j)>98
            Avg_intensity_3(i,j)=nanmean(INTENSITY_3(i,j,:),3);
        else
            Avg_intensity_3(i,j)=NaN;
        end
    end
end
for i=1:sy
    for j=1:sx
        if sumtempbin_4(i,j)>98
            Avg_intensity_4(i,j)=nanmean(INTENSITY_4(i,j,:),3);
        else
            Avg_intensity_4(i,j)=NaN;
        end
    end
end
for i=1:sy
    for j=1:sx
        if sumtempbin_5(i,j)>98
            Avg_intensity_5(i,j)=nanmean(INTENSITY_5(i,j,:),3);
        else
            Avg_intensity_5(i,j)=NaN;
        end
    end
end

Avg_intensity_1(Avg_intensity_1<100)=NaN;

```

```

Avg_intensity_2(Avg_intensity_2<100)=NaN;
Avg_intensity_3(Avg_intensity_3<100)=NaN;
Avg_intensity_4(Avg_intensity_4<100)=NaN;
Avg_intensity_5(Avg_intensity_5<100)=NaN;

[Y_s,X_s]=size(Avg_intensity_1);
X_loc=1:X_s;
Y_loc=1:Y_s;
% RE-ASSIGN LOCATION OF AVERAGE TEMPERATURE FROM PIXEL TO IGNITER DIAMETERS
% IGNITER CENTER AT (35,7)
X_center=((X_loc-35)/1.74)/12.88; % 12.88 IS THE DIAMETER OF IGNITER
Y_center=((Y_loc-7)/1.74)/12.88; % 1.74 IS RESOLUTION (PIX/MM)

figure
contourf(X_center,Y_center,rot90(Avg_intensity_1,2),50,'edgecolor','none')
v = colorbar;
ylabel(v,'Temperature [K]')
caxis([600 1200]);
axis equal
xlim([-1 1])
ylim([0 3])
colormap jet
title('0.6 ms')
xlabel('x/D')
ylabel('y/D')
set(gca,'fontsize',24)
v.Visible='off';

figure
contourf(X_center,Y_center,rot90(Avg_intensity_2,2),50,'edgecolor','none')
v = colorbar;
ylabel(v,'Temperature [K]')
caxis([600 1000]);
axis equal
xlim([-1 1])
ylim([0 3])
colormap jet
title('1.3 ms')
xlabel('x/D')
set(gca,'fontsize',24)
set(gca,'YTickLabel',[])
v.Visible='off';

figure
contourf(X_center,Y_center,rot90(Avg_intensity_3,2),50,'edgecolor','none')
v = colorbar;
ylabel(v,'Temperature [K]')
caxis([600 1000]);
axis equal
xlim([-1 1])
ylim([0 3])
colormap jet
title('2.0 ms')
xlabel('x/D')
set(gca,'fontsize',24)

```

```

set(gca,'YTickLabel',[])
v.Visible='off';

figure
contourf(X_center,Y_center,rot90(Avg_intensity_4,2),50,'edgecolor','none')
v = colorbar;
v.Visible='off';
ylabel(v,'Temperature [K]')
caxis([600 1000]);
axis equal
xlim([-1 1])
ylim([0 3])
colormap jet
title('2.6 ms')
xlabel('x/D')
set(gca,'fontsize',24)
set(gca,'YTickLabel',[])

figure
contourf(X_center,Y_center,rot90(Avg_intensity_5,2),50,'edgecolor','none')
v = colorbar;
ylabel(v,'Temperature [K]')
caxis([600 1000]);
axis equal
xlim([-1 1])
ylim([0 3])
colormap jet
title('3.3 ms')
xlabel('x/D')
set(gca,'fontsize',24)
set(gca,'YTickLabel',[])

%%%% PLOTTING KERNEL CENTROIDS %%%
% THIS CODE WILL OUTPUT A DISTRIBUTION OF KERNELS WITH 95% SPREAD
% IN QUIESCENT CONDITIONS

clear
clc

% LOAD COORDINATES OF DETECTED CENTROIDS DETERMINED IN DIT CODE
n_1=load('Centroid_final_518.mat');
n_2=load('Centroid_final_519.mat');
n_3=load('Centroid_final_520.mat');
n_4=load('Centroid_final_527.mat');
n_13=load('Centroid_final_521.mat');
n_14=load('Centroid_final_526.mat');
n_15=load('Centroid_final_528.mat');
n_16=load('Centroid_final_529.mat');

n_9=load('Centroid_final_535.mat');
n_10=load('Centroid_final_536.mat');
n_11=load('Centroid_final_537.mat');
n_17=load('Centroid_final_538.mat');

```

```

n_18=load('Centroid_final_319.mat');
n_19=load('Centroid_final_320.mat');
n_20=load('Centroid_final_328.mat');
n_21=load('Centroid_final_329.mat');

% ASSIGN LOCATION ARRAYS FROM .MAT FILE
T_1=n_1.cent_roid;
z1=size(T_1,3);
T_2=n_2.cent_roid;
z2=size(T_2,3);
T_3=n_3.cent_roid;
z3=size(T_3,3);
T_4=n_4.cent_roid;
z4=size(T_4,3);
T_13=n_13.cent_roid;
z13=size(T_13,3);
T_14=n_14.cent_roid;
z14=size(T_14,3);
T_15=n_15.cent_roid;
z15=size(T_15,3);
T_16=n_16.cent_roid;
z16=size(T_16,3);

T_9=n_9.cent_roid;
T_9=circshift(T_9, [0 -2]); % THIS LINE ENSURES THAT THE ORIGIN OF THE
% IGNITER IS UNIFORM ACROSS ALL DATA SETS
z9=size(T_9,3);
T_10=n_10.cent_roid;
T_10=circshift(T_10, [0 -2]);
z10=size(T_10,3);
T_11=n_11.cent_roid;
T_11=circshift(T_11, [0 -2]);
z11=size(T_11,3);
T_17=n_17.cent_roid;
T_17=circshift(T_17, [0 -2]);
z17=size(T_17,3);

T_18=n_18.cent_roid;
z18=size(T_18,3);
T_19=n_19.cent_roid;
z19=size(T_19,3);
T_20=n_20.cent_roid;
z20=size(T_20,3);
T_21=n_21.cent_roid;
z21=size(T_21,3);

% CONCATENATE LOCATIONS IN 2ND DIMENSION
T=single(cat(2,T_1,T_2,T_3,T_4,T_13,T_14,T_15,T_16,T_9,T_10,T_11,T_17,T_18,T_
19,T_20,T_21));

TX=T(1,:);
TY=T(2,:);

```

```

[Y_s,X_s]=size(T);
X_loc=1:X_s;
Y_loc=1:Y_s;

% SORT LOCATIONS IN ASCENDING VERTICAL DIRECTION
[Y_centroid, Sortindex]=sort(TY);
X_centroid=TX(Sortindex); % CORRESPONDING X LOCATION FROM Y SORT

for i=1:length(X_centroid)
    X_2(i)=X_centroid(length(X_centroid)-i+1); % THIS LINE INVERTS THE
    % ORDER OF THE DATA POINTS, THIS IS NEEDED FOR DETERMINING 95% SPREAD
end

% CENTER AT (56,62)
X_center=((X_2-56)/1.74)/12.88;
Y_center=((Y_centroid-7)/1.74)/12.88;

vert=linspace(0,2.5,10);

% DETERMINE 95% SPREAD
combine=[Y_center;X_center];
dist(2,1)=std(X_center(1:9)); % .25D
dist(2,2)=std(X_center(10:113)); % .5D
dist(2,3)=std(X_center(114:434)); % .75D
dist(2,4)=std(X_center(435:899)); % 1D
dist(2,5)=std(X_center(900:1349)); % 1.25D
dist(2,6)=std(X_center(1350:1713)); % 1.5D
dist(2,7)=std(X_center(1714:1994)); % 1.75D
dist(2,8)=std(X_center(1995:2049)); % 2D
dist(1,:)=.25:.25:2;
dist(2,:)=2*dist(2,:);

St_d95=std(Y_center)*2;
Avg=mean(Y_center);

x95=0:.1:max(Avg+St_d95);
% SLOPE OF 95% SPREAD USING THE STD VALUES DETERMINED ABOVE
y95=.42*x95+.015;
ym95=-.42*x95-.015;

figure
plot(Y_center,X_center,'x')
axis equal
hold on
plot(x95,y95,'r:','LineWidth',3)
hold on
plot(x95,ym95,'r:','LineWidth',3)
xlim([0 3])
ylim([-1 1])
xlabel('y/D')
ylabel('x/D')
set(gca,'fontsize',24)
camroll(90)
set(gca,'XAxisLocation','top')

```

```

%%%% AVERAGE KERNEL VELOCITY %%%
% THIS CODE WILL OUTPUT THE PHASE VELOCITIES OF KERNELS IN QUIESCENT
% CONDITIONS

clear
clc

% LOAD TEMPERATURE .MAT FILES DETERMINED FROM DIT CODE
n_1=load('Centroid_final_partial_518.mat');
n_2=load('Centroid_final_partial_519.mat');
n_3=load('Centroid_final_partial_520.mat');
n_4=load('Centroid_final_partial_527.mat');
n_13=load('Centroid_final_partial_521.mat');
n_14=load('Centroid_final_partial_526.mat');
n_15=load('Centroid_final_partial_528.mat');
n_16=load('Centroid_final_partial_529.mat');

n_9=load('Centroid_final_partial_535.mat');
n_10=load('Centroid_final_partial_536.mat');
n_11=load('Centroid_final_partial_537.mat');
n_17=load('Centroid_final_partial_538.mat');

n_18=load('Centroid_final_partial_319.mat');
n_19=load('Centroid_final_partial_320.mat');
n_20=load('Centroid_final_partial_328.mat');
n_21=load('Centroid_final_partial_329.mat');

T_1=n_1.cent_roid_pre';
T_2=n_2.cent_roid_pre';
T_3=n_3.cent_roid_pre';
T_4=n_4.cent_roid_pre';
T_13=n_13.cent_roid_pre';
T_14=n_14.cent_roid_pre';
T_15=n_15.cent_roid_pre';
T_16=n_16.cent_roid_pre';
T_9=n_9.cent_roid_pre';
T_10=n_10.cent_roid_pre';
T_11=n_11.cent_roid_pre';
T_17=n_17.cent_roid_pre';
T_18=n_18.cent_roid_pre';
T_19=n_19.cent_roid_pre';
T_20=n_20.cent_roid_pre';
T_21=n_21.cent_roid_pre';

T_pre=single(cat(1,T_1,T_2,T_3,T_4,T_13,T_14,T_15,T_16,T_9,T_10,T_11,T_17,T_1
8,T_19,T_20,T_21));

% SEPARATE XY COORDINATES BASED ON SPARK EVENT
T_x=reshape(T_pre(:,1),5,[]);
T_y=reshape(T_pre(:,2),5,[]);

```

```

for i=1:size(T_x,2)
for j=1:size(T_x,1)-1
if T_y(j+1,i)>T_y(j,i) % IF VERTICAL HEIGHT OF KERNEL WAS SMALLER THAN
    % PREVIOUS LOCATION, NaN REMAINING COORDINATES (NOTE: > IS USED BECAUSE
    % OF KERNELS EJECTING IN THE DOWNWARD NORMAL)
    T_x(j:end,i)=nan;
    T_y(j:end,i)=nan;
end
end
end

for i=1:size(T_x,2)
for j=1:size(T_x,1)
if T_x(j,i)==0
    T_x(j:end,i)=nan;
    T_y(j:end,i)=nan;
end
end
end

T_1_xxx=T_x(1,:);
T_1_yyy=T_y(1,:);
% INITIAL KERNEL VELOCITY AFTER DISCHARGE
x_o=56; % ASSUMED THAT KERNELS EJECT FROM CENTER OF IGNITER
y_o=51.4; % HEIGHT OF KERNEL AFTER PLASMA WAS NO LONGER DETECTED, THIS WAS
% STATISTICALLY FOUND, SEE EXCEL SHEET NAMED "velocity_intial image_v2.
% xlsx"
vel_mag(1,:)=sqrt(((T_1_xxx-56)/.000667).^2+((T_1_yyy-y_o)/.000667).^2);
% RESULTANT VELOCITY
velocity(1,:)=vel_mag(1,:)/1.74/1000; % CONVERT TO M/S

% KERNEL VELOCITY LATER IN TIME
for j=2:size(T_y,1)
    for i=1:size(T_x,2)

vel_mag=sqrt(((T_x(j,i)-T_x(j-1,i))/0.000667).^2+((T_y(j,i)-T_y(j-
1,i))/0.000667).^2);
velocity(j,i)=vel_mag/1.74/1000;
% vel_

        end
    end

disp(nanmean(velocity,2))
disp(nanstd(velocity(1,:)))
disp(nanstd(velocity(2,:)))
disp(nanstd(velocity(3,:)))
disp(nanstd(velocity(4,:)))
disp(nanstd(velocity(5,:)))

```

**"! RADIATIVE LOSSES OF TYPE B THERMOCOUPLE"**

" This code will output the temperature of a McKenna burner flame given thermocouple data "

D=0.3\*convert(mm,m) "TC diamter bead, source: Hindasageri et al. pg 9"

sigma=5.67E-8 "Stefan-Boltzmann constant"

P\_inf=101300 "Ambient pressure"

T\_inf=295 "Ambient temperature"

Re\_D=rho\_f\*V\_mix\*D/mu\_f "Reynolds number over TC bead"

rho\_f=Density(Air,T=T\_f,P=P\_inf) "Density at flame temp."

Q\_mix=10000\*((1/100)^3)\*(1/60) "10,000 SCCM to m^3/sec"

D\_mck=60\*convert(mm,m)

A\_mck=pi/4\*(D\_mck^2)

V\_mix=Q\_mix/A\_mck

mu\_f=Viscosity(Air,T=T\_f)

"NU=C\*(Re\_D^m)\*(Pr^(1/3))"

C=.989

"Correlations from Incropera"

m=.33

A\_s=pi\*D^2

" Heat transfer Equations "

Pr=c\_p\_f\*mu\_f/k\_f

NU=h\*D/k\_f

NU=.42\*(Pr^.2)+.57\*(Pr^(1/3))\*(Re\_D^.5)

"pg. 179 of Viscous Flow"

Q\_conv=h\*A\_s\*(T\_f-T\_tc)

Q\_rad=A\_s\*sigma\*epsilon\*(T\_tc^4-T\_inf^4)

Q\_conv=Q\_rad

epsilon=(6E-5)\*T\_f+.0138

"Source: Hindasageri et al. pg. 6"

Rad\_loss=(1-T\_tc/T\_f)\*100

Pe=Re\_D\*Pr

" Use a Parametric Table and manually input T\_tc, cp\_f, and k\_f "

" cp\_f and k\_f surpass the database within EES at the temperatures measured "